Magneto-optical Hall response in generic Weyl semimetals

Marcus Ståhammar*

Nordita, KTH Royal Institute of Technology and Stockholm University, Hannes Alfvéns väg 12, SE-106 91 Stockholm, Sweden

(Received 24 February 2024; revised 19 April 2024; accepted 17 June 2024; published 1 July 2024)

Weyl semimetals are predicted to host signature magneto-optical properties sourced by their peculiar Landau-level structure, including the chiral level. Analytical studies are often leaving out the Hall component of the conductivity due to its complicated nature, and even though the chiral anomaly requires Weyl nodes to come in charge-conjugate pairs, toy models hosting only one node are considered almost exclusively; numerical studies including several Weyl nodes are, on the other hand, often limited to high-field quantum limits or dc studies. Here, we present a twofold purpose study, where we (a) analytically derive a closed-form expression also for the Hall conductivity of a generic Weyl semimetal using linear response theory and (b) apply this general framework to evaluate the transverse conductivity components for Weyl systems with two nodes. We study how various model parameters, including the tilt, momentum separation, and energy location of the nodes, as well as the chemical potential, affect the magneto-optical conductivity, and complement these studies by deriving an analytical expression for the dc Hall conductivity, which is also evaluated in various systems. Including a chiral pair of nodes results in two important differences compared to earlier studies: the contribution from the chiral level is equal in size but opposite at the two nodes, making the net contribution disappear, and the energy scales at which intraband transitions occur is smeared out and approaches that of interband transitions, strengthening the hypothesis that intraband transitions mask signature optical features in materials. This general formalism can be applied to a large family of generic Weyl semimetals, and comprise an important piece towards unravelling the source of the mismatch between theoretical predictions and experimental observations in candidate materials.

DOI: 10.1103/PhysRevB.110.035401

I. INTRODUCTION

Topological phases of matter have been extensively studied both from a theoretical and experimental perspective since the observation of the quantum Hall effect in the 1980s [1]. This has resulted in the tenfold way classification [2], a thorough framework for understanding gapped topological insulators [3] and superconductors [4] as well as gapless systems as the semimetallic state of graphene in two dimensions [5] and Weyl semimetals in three dimensions [6]. Apart from proving fruitful within condensed matter physics, these studies have profound consequences in other areas of physics, where one paramount example is the realization of Weyl fermions as quasiparticle excitations in the vicinity of the pointlike band intersections in Weyl semimetals [7–9]; these elusive particles were originally theoretically predicted by Hermann Weyl in 1929 in the context of particle physics [10], and have yet to be observed as actual fundamental particles. The intersections, naturally known as Weyl points or Weyl nodes, appear in two different types distinguished by the behavior of the dispersion in the vicinity of the degeneracy [6]. In type-I systems, the valence and conduction bands merely touch the Fermi level, forming a proper semimetallic state with a pointlike Fermi surface [11–13], while type-II nodes come with a finite Fermi surface as a consequence of the dispersion being overtilted [14,15].

The existence of Weyl nodes have furthermore indicated that Weyl semimetals ought to host unique transport properties related to electromagnetic response. Salient examples are negative magnetoresistence [16–18] and the chiral anomaly [11,19–29], but do also include signature magneto-optical properties. The magneto-optical conductivity, for example, is predicted to host a series of asymmetrically spaced peaks caused by optical transitions between Landau levels [30–33], something that initially was believed to work as an experimental signature identifying Weyl semimetals [6]. Nowadays, it is known that theoretical predictions are at odds with experimental observations [34–36], something that has been suggested is due to the existence of trivial Fermi pockets, i.e., regions where the bands cross the Fermi level not in direct connection to a Weyl node [32].

Studies on magneto-optical transport properties in Weyl semimetals are usually carried out with two rather different approaches. Either simplified pictures including systems with only one Weyl node are studied analytically [30–33,37–40] or the studies rely exclusively on numerical simulations of lattice systems; see Ref. [41] for a recent study. Additional examples include conductivity in Weyl semimetal sheets [42], high-field quantum limits [43], and magneto-optical transport in the

*Contact author: marcus.stalhammar@su.se

dc-limit [44–46]. All these works have provided fruitful insights regarding transport phenomena and the quantum Hall effect in three dimensions, but in one way or the other lack either a realistic or generic setup. Therefore, in this paper, we investigate the effects of having systems with a chiral pair of Weyl nodes, including fourth-order momentum terms in the dispersion. We investigate how the interplay between the nodes, such as its tilts and position in energy and momentum space, affect the transport properties, and also how these are connected to the appearance of trivial and nontrivial Fermi pockets. We go further beyond previous studies by expanding the general analytical framework developed in Ref. [32], where a closed-form expression for the dissipative components of the conductivity tensor are derived, to also include the reactive components. This allows us to not only study transport in terms of the real part of σ_{xx}, but also the Hall conductivity, the real part of σ_{xy}, at any frequencies. Through the same technique, we also analytically derive the dc Hall conductivity and display how these analytical expressions serve as a tool for predicting physical features directly from the band structure.

The paper shows that a charge-conjugate pair of Weyl nodes causes the contribution from the chiral level to cancel, and further indicates that the energy scales at which intraband transitions appear are smeared out, strengthening the hypothesis that these are responsible for the disagreements between theory and experiments. This analytical framework thus comprises a natural step towards an agreement between theory and experiment and can, in principle, work as a tool to make transport predictions for material candidates as long as the corresponding band structure is provided (e.g., using DFT). It furthermore contributes to an increased and more complete theoretical understanding of transport features in three dimensions, including the three-dimensional quantum Hall effect, thanks to the corresponding analytical expressions for the respective quantity.

The rest of the paper is structured as follows. We set the stage in Sec. II and combine a brief background of previous works and analytical techniques with unique calculations and derivations. In particular, we show how the Landau-level splitting works in generic Weyl systems and provide a simplification of the expressions for the dissipative conductivity components before we turn to deriving the closed-form expressions for the corresponding reactive components and the dc Hall conductivity. In Sec. III, the formalism is applied to various Weyl systems with two Weyl nodes. We investigate how the tilt of the respective nodes, and hence the presence of trivial and nontrivial Fermi pockets, is manifest in transport. In particular, we study the different features present in the type-I and type-II regimes to try to identify the interplay between these two regimes. We discuss the results and their relevance in Sec. IV and provide additional plots for when the two Weyl nodes are at different energies and for the corresponding dc conductivity. We summarize and conclude in Sec. V.

II. MAGNETO-OPTICAL CONDUCTIVITY FOR GENERIC WEYL SEMIMETALS

We devote Secs. II A and II B to set the stage and describe how the Landau-level quantization works in a family of generic Weyl semimetals, and recall the derivation of the dissipative components of the conductivity tensor carried out in Ref. [32] (which is also further simplified). In Sec. II C, we also carry out the analytical derivation of a convenient closed-form expression for the reactive components, including the magneto-optical Hall conductivity, and apply these techniques also in the dc-limit in Sec. II D.

A. Landau-level quantization

Take as starting point a generalized Weyl Hamiltonian,

$$\mathcal{H} = \hbar v_F [h(k_z)\sigma^0 + k_x\sigma^x + k_y\sigma^y + g(k_z)\sigma^z], \tag{1}$$

where $\mathbf{k} = (k_x, k_y, k_z)$ is the lattice momentum, $\boldsymbol{\sigma} = (\sigma^x, \sigma^y, \sigma^z)$ the Pauli matrices, σ^0 the 2×2 identity matrix, v_F the Fermi velocity, and $h(k_z)$ and $g(k_z)$ continuously differentiable functions of k_z only. The function $h(k_z)$ introduces a tilt in the k_z direction and $g(k_z)$ specifies the position of the Weyl nodes in the spectrum.

To study magneto-optical transport, we couple the Hamiltonian to an external magnetic field through minimal coupling. For concreteness, the magnetic field is aligned with the direction of the tilt, i.e., $\mathbf{B} = (0, 0, B)$, which in the Landau gauge corresponds to introducing a vector potential of the form $\mathbf{A} = (0, Bx, 0)$. The minimal coupling transforms the momentum as $\hbar k_i \to \Pi_i = \hbar k_i - \frac{e}{c}A_i$. By introducing creation and annihilation operators as $a = \frac{l_B}{\sqrt{2}\hbar}(\Pi_x - i\Pi_y)$ and $a^\dagger = \frac{l_B}{\sqrt{2}\hbar}(\Pi_x + i\Pi_y)$, which satisfy $[a, a^\dagger] = 1$, the system under the influence of a magnetic field can be effectively described by

$$H = \hbar v_F \begin{pmatrix} h(k_z) + g(k_z) & \frac{\sqrt{2}}{l_B}a^\dagger \\ \frac{\sqrt{2}}{l_B}a & h(k_z) - g(k_z) \end{pmatrix}. \tag{2}$$

The corresponding eigenvalues are

$$E_{n,\lambda}(k_z, l_B) = \hbar v_F \left[h(k_z) + \lambda \sqrt{g^2(k_z) + \frac{2n}{l_B^2}} \right], \quad n \geqslant 1, \tag{3}$$

$$E_0(k_z) = \hbar v_F [h(k_z) + g(k_z)], \tag{4}$$

with $\lambda = \pm 1$, and the eigenstates cast the form $\psi_{n,\lambda}(k_z, l_B) = \begin{pmatrix} \lambda u_{n,\lambda}(k_z, l_B) \\ v_{n,\lambda}(k_z, l_B) \end{pmatrix}$, with

$$u_{n,\lambda}(k_z, \mathfrak{l}_B) = \sqrt{\frac{1}{2}\left[1 + \frac{g(k_z)}{\lambda\sqrt{g^2(k_z) + \frac{2n}{l_B^2}}}\right]}, \quad n \geqslant 1, \tag{5}$$

$$v_{n,\lambda}(k_z, \mathfrak{l}_B) = \sqrt{\frac{1}{2}\left[1 - \frac{g(k_z)}{\sqrt{g^2(k_z) + \frac{2n}{l_B^2}}}\right]}, \quad n \geqslant 1, \tag{6}$$

$$\psi_0 = \begin{pmatrix} 1 \\ 0 \end{pmatrix}. \tag{7}$$

B. Dissipative components of the response function

The magneto-optical conductivity is, in the one-loop approximation, calculated using linear response theory and specifically expressed in terms of the response function (in what follows, we will omit certain dependencies of parameters, and reintroduce them when

appropriate),

$$\chi_{\mu\nu}(\omega) = \frac{1}{2\pi l_B^2} \sum_{n,n'} \sum_{\lambda,\lambda'} \int_{-\infty}^{+\infty} \frac{dk_z}{2\pi} \frac{f[E_{n,\lambda}(k_z)] - f[E_{n',\lambda'}(k_z)]}{\hbar\omega + E_{n,\lambda}(k_z) - E_{n',\lambda'}(k_z) + i\epsilon} \langle\psi_{n,\lambda}(k_z)|j_\mu|\psi_{n',\lambda'}(k_z)\rangle \langle\psi_{n',\lambda'}(k_z)|j_\nu|\psi_{n,\lambda}(k_z)\rangle, \tag{8}$$

with $f(E) = \frac{1}{1+e^{\beta(E-\mu)}}$ the Fermi-Dirac distribution, $\beta^{-1} = k_B T$, T the temperature, and k_B the Boltzmann constant. Small, but finite, and positive ϵ regulates the integral, and can be thought of as an inverse impurity scattering lifetime τ via $\epsilon = \frac{\hbar}{2\tau}$. The current operators j_μ are given by

$$j_\mu = \frac{e}{\hbar} \frac{\partial H}{\partial \Pi_\mu}. \tag{9}$$

In Ref. [32], analytical expressions for the dissipative parts of $\chi_{xx}(\omega)$ and $\chi_{xy}(\omega)$ for generic Weyl systems were derived. We do not repeat this derivation here, but instead further simplify these expressions, with the final goal of also deriving a closed-form analytical expression for the reactive parts of the response function. The final result of Ref. [32] can, after some straight-forward algebra, be put in the form

$$\begin{aligned}
\mathrm{Im}[\chi_{xx}(\omega)] = -\frac{e^2 v_F^2}{16\pi l_B^2} \sum_{n=0}^{n_{\max}} \sum_{i=1}^{2m} \Bigg\{ & A_n^{++}(k_i) \left[\frac{\frac{2n+1}{l_B^2} - \frac{\omega^2}{2v_F^2}}{|\tilde{g}(k_i) g'(k_i)|} \right] \theta\left(\frac{2v_F^2}{l_B^2} - \omega^2 \right) \mathrm{sgn}(-\omega) \\
& + A_n^{--}(k_i) \left[\frac{\frac{2n+1}{l_B^2} - \frac{\omega^2}{2v_F^2}}{|\tilde{g}(k_i) g'(k_i)|} \right] \theta\left(\frac{2v_F^2}{l_B^2} - \omega^2 \right) \mathrm{sgn}(\omega) + A_n^{+-}(k_i) \left[\frac{\frac{\omega^2}{2v_F^2} - \frac{2n+1}{l_B^2}}{|\tilde{g}(k_i) g'(k_i)|} \right] \theta\left(\omega^2 - \frac{2v_F^2}{l_B^2} \right) \mathrm{sgn}(\omega) \\
& + A_n^{-+}(k_i) \left[\frac{\frac{\omega^2}{2v_F^2} - \frac{2n+1}{l_B^2}}{|\tilde{g}(k_i) g'(k_i)|} \right] \theta\left(\omega^2 - \frac{2v_F^2}{l_B^2} \right) \mathrm{sgn}(-\omega) \Bigg\},
\end{aligned} \tag{10}$$

$$\begin{aligned}
\mathrm{Re}[\chi_{xy}(\omega)] = -\frac{e^2 v_F^2}{16\pi l_B^2} \sum_{n=0}^{n_{\max}} \sum_{i=1}^{2m} \Bigg\{ & A_n^{++}(k_i) \left[\frac{\frac{2n+1}{l_B^2} - \frac{\omega^2}{2v_F^2}}{|\tilde{g}(k_i) g'(k_i)|} \right] \theta\left(\frac{2v_F^2}{l_B^2} - \omega^2 \right) \\
& + A_n^{--}(k_i) \left[\frac{\frac{2n+1}{l_B^2} - \frac{\omega^2}{2v_F^2}}{|\tilde{g}(k_i) g'(k_i)|} \right] \theta\left(\frac{2v_F^2}{l_B^2} - \omega^2 \right) + A_n^{+-}(k_i) \left[\frac{\frac{\omega^2}{2v_F^2} - \frac{2n+1}{l_B^2}}{|\tilde{g}(k_i) g'(k_i)|} \right] \theta\left(\omega^2 - \frac{2v_F^2}{l_B^2} \right) \\
& + A_n^{-+}(k_i) \left[\frac{\frac{\omega^2}{2v_F^2} - \frac{2n+1}{l_B^2}}{|\tilde{g}(k_i) g'(k_i)|} \right] \theta\left(\omega^2 - \frac{2v_F^2}{l_B^2} \right) \Bigg\},
\end{aligned} \tag{11}$$

with

$$g(k_i) = \pm \sqrt{\frac{v_F^2}{\omega^2 l_B^4} - \frac{2n+1}{l_B^2} + \frac{\omega^2}{4v_F^2}}, \tag{12}$$

$$\tilde{g}(k_i) = \left| \frac{\omega}{v_F} \right| g(k_i), \tag{13}$$

$$A_n^{\lambda\lambda'}(k_i) = f[E_{n,\lambda}(k_i)] - f[E_{n+1,\lambda'}(k_i)], \tag{14}$$

$$n_{\max} = \left\lfloor \frac{\left(2v_F^2 - \omega^2 l_B^2\right)^2}{8 v_F^2 \omega^2 l_B^2} \right\rfloor, \tag{15}$$

$\theta(x)$ the Heaviside step function, and k_i the value of k_z that satisfies Eq. (12). We devote the Appendix to the calculational details. Here it is important to keep in mind that $g(k_i)$ and k_i, and hence also $g'(k_i)$, are bound to be real, otherwise they do not represent the physical problem we are considering; they are forced to be real since $g(k_z)$ appear in the energy eigenvalues in Eqs. (3) and (4). This will be important later on. Further note that $h(k_z)$ enters through the factors $A_n^{\lambda\lambda'}$, since their definition includes the dispersion relation.

The Kramers-Kronig relations tells us that the reactive and dissipative components of the response functions are given in terms of each other as

$$\mathrm{Re}[\chi_{\mu\nu}(\omega)] = \mathrm{PV} \int_{-\infty}^{+\infty} \frac{d\omega'}{\pi} \frac{\mathrm{Im}[\chi_{\mu\nu}(\omega')]}{\omega' - \omega}, \tag{16}$$

$$\mathrm{Im}[\chi_{\mu\nu}(\omega)] = -\mathrm{PV} \int_{-\infty}^{+\infty} \frac{d\omega'}{\pi} \frac{\mathrm{Re}[\chi_{\mu\nu}(\omega')]}{\omega' - \omega}, \tag{17}$$

where PV denotes the Cauchy principal value of the corresponding integral. This means that to derive analytical expressions for $\mathrm{Re}[\chi_{xx}(\omega)]$ and $\mathrm{Im}[\chi_{xy}(\omega)]$, respectively, we need to evaluate the corresponding principal value integrals. This will be the topic of the following subsection. Finally, the conductivity tensor is given by the Kubo formula:

$$\sigma_{\mu\nu}(\omega) = \frac{1}{i\omega}[\chi_{\mu\nu}(\omega) - \chi_{\mu\nu}(0)]. \tag{18}$$

For generic Weyl systems, the Landau levels are completely nondegenerate, meaning that $E_{n,\lambda}(k_z) \neq E_{n',\lambda'}(k_z)$ for every $n \neq n'$, every λ and λ', and all k_z. Therefore, $\chi_{\mu\nu}(0)$ will vanish in the clean limit, $\epsilon \to 0$, and for $\omega \neq 0$, the conductivity components for clean Weyl systems can be put in the form

$$\begin{aligned}\sigma_{xx}(\omega) &= \frac{1}{\omega}\{\mathrm{Im}[\chi_{xx}(\omega)] - i\mathrm{Re}[\chi_{xx}(\omega)]\} \\ &= \frac{1}{\omega}\left\{\mathrm{Im}[\chi_{xx}(\omega)] - i\mathrm{PV}\int_{-\infty}^{+\infty}\frac{d\omega'}{\pi}\frac{\mathrm{Im}[\chi_{xx}(\omega')]}{\omega'-\omega}\right\},\end{aligned} \tag{19}$$

$$\begin{aligned}\sigma_{xy}(\omega) &= \frac{1}{\omega}\{\mathrm{Im}[\chi_{xy}(\omega)] - i\mathrm{Re}[\chi_{xy}(\omega)]\} \\ &= -\frac{1}{\omega}\left\{\mathrm{PV}\int_{-\infty}^{+\infty}\frac{d\omega'}{\pi}\frac{\mathrm{Re}[\chi_{xy}(\omega')]}{\omega'-\omega} + i\mathrm{Re}[\chi_{xy}(\omega)]\right\}.\end{aligned} \tag{20}$$

This makes it clear that to obtain the Hall conductivity, the principal value has to be computed, which is the main motivation for finding a closed-form expression for it.

C. Reactive components of the response function

The reactive components of the response functions are directly related to the dissipative components through the Kramers-Kronig relations, Eqs. (16) and (17). To evaluate the corresponding principal values, we first consider the zero-temperature limit, where the factors $A_n^{\lambda\lambda'}(k_i)$ are

$$A_n^{\lambda\lambda'}(k_i) \xrightarrow{T\to 0} \theta[\mu - E_{n,\lambda}(k_i)] - \theta[\mu - E_{n+1,\lambda'}(k_i)]. \tag{21}$$

In this limit, the dissipative components of the response functions will host singularities only when $\omega' = \omega$ when $g[k_i(\omega', n)] = 0$, or when $g'[k_i(\omega', n)] = 0$. The singularity at $\omega' = \omega$ is a simple pole located at the real axis, while the remaining singularities are square-root branch points, the location of which we need to identify. For this, we first recall that for causality reasons, the response function is analytic in the upper half complex ω-plane, meaning that for $\mathrm{Im}(\omega') > 0$, $\chi_{\mu\nu}(\omega')$ is analytic. Furthermore, the branch points related to $g[k_i(\omega', n)] = 0$ and $g'[k_i(\omega', n)] = 0$ necessarily come in respective complex conjugate pairs, since both $g(k_i)$ and $g'(k_i)$ are purely real [recall that $g(k_z)$ defines the energy eigenvalues, which are bound to be real]. But since there are no poles in the upper half complex ω' plane, $g = 0$ and $g' = 0$ cannot be satisfied for any complex ω'. This means that all singularities, both poles and branch cuts, are constrained to the real line. Using this along with the relations

$$\begin{aligned}&\mathrm{PV}\int_{-\infty}^{+\infty}\frac{d\omega'}{\pi}\frac{\mathrm{Re}[\chi_{\mu\nu}(\omega')]}{\omega'-\omega} \\ &\quad= \frac{1}{2}\int_{-\infty}^{+\infty}\frac{d\omega'}{\pi}\left\{\frac{\mathrm{Re}[\chi_{\mu\nu}(\omega')]}{\omega'-\omega-i\epsilon} + \frac{\mathrm{Re}[\chi_{\mu\nu}(\omega')]}{\omega'-\omega+i\epsilon}\right\},\end{aligned} \tag{22}$$

$$\begin{aligned}&\mathrm{PV}\int_{-\infty}^{+\infty}\frac{d\omega'}{\pi}\frac{\mathrm{Im}[\chi_{\mu\nu}(\omega')]}{\omega'-\omega} \\ &\quad= \frac{1}{2}\int_{-\infty}^{+\infty}\frac{d\omega'}{\pi}\left\{\frac{\mathrm{Im}[\chi_{\mu\nu}(\omega')]}{\omega'-\omega-i\epsilon} + \frac{\mathrm{Im}[\chi_{\mu\nu}(\omega')]}{\omega'-\omega+i\epsilon}\right\},\end{aligned} \tag{23}$$

the principal values can be evaluated using contour integration techniques. To do this properly, we first need to specify what branch cuts to use. This will depend on the value of ω. Denoting the branch points as ω_i, they form the set $\{\omega_j\}_{j=1}^{2m}$ and are ordered such that $\omega_j < \omega_{j+1}$ for all j. Then, we will have the following two different cases:

(1) If $\omega < \omega_1$, or $\omega_{2m} < \omega$, or $\omega_1 < \ldots < \omega_{2a} < \omega < \omega_{2a+1} < \ldots < \omega_{2m}$ for some $1 < a < m-1$, the branch cuts are formed between neighboring branch points, i.e., all branch cuts are finite and made between ω_{2j-1} and ω_{2j} for $j = 1, \ldots, m$.

(2) If $\omega_1 < \ldots < \omega_{2a-1} < \omega < \omega_{2a+1} < \ldots < \omega_{2m}$ for some $1 < a < m-1$, we have infinite branch cuts on the interval $(-\infty, \omega_1]$ and $[\omega_{2m}, +\infty)$, and finite branch cuts between neighboring pairs ω_{2j} and ω_{2j+1} for $1 < j < m-1$.

These are schematically depicted with the resulting integration contours in Fig. 1.

Knowing where the branch cuts are located, we can now specify what contour to use. The first integral in Eqs. (22) and (23) is evaluated by first surrounding the branch cuts with semicircular arcs of radius r in the upper half plane, the pole at $\omega' = \omega$ with a semicircular arc of radius r in the lower half plane, and then closing the contour with a semicircular arc of radius R in the lower half plane. Deforming this contour, we end up with a series of dogbone or dumbell contours, and potentially a pair of hairpin contours (if the branch cuts to infinity are present) wrapping around the branch cuts, as depicted in Figs. 1(c) and 1(f). The second integral in Eqs. (22) and (23) is evaluated by first surrounding the branch points with semicircular arcs of radius r in the upper half plane, the pole at $\omega' = \omega$ with a semi circular arc of radius r in the upper half plane, and then closing the contour with a semicircular arc of radius R in the upper half plane. This contour will vanish completely upon deformation. Using the Residue theorem and the Estimation lemma method to show that the contribution from all semicircular arcs around the branch points and from the infinite arc vanish when $r \to 0$, and $R \to \infty$, respectively, we finally arrive at

$$\begin{aligned}\mathrm{Re}[\chi_{xx}(\omega)] &= \mathrm{PV}\int_{-\infty}^{\infty}\frac{d\omega'}{\pi}\frac{\mathrm{Im}[\chi_{xx}(\omega')]}{\omega'-\omega} \\ &= \begin{cases}\sum_{j=1}^{m}\int_{\omega_{2j-1}}^{\omega_{2j}}\frac{d\omega'}{\pi}\frac{\mathrm{Im}[\chi_{xx}(\omega')]}{\omega'-\omega}, & \omega \text{ has even number of poles to the left} \\ \int_{-\infty}^{\omega_1}\frac{d\omega'}{\pi}\frac{\mathrm{Im}[\chi_{xx}(\omega')]}{\omega'-\omega} + \int_{\omega_{2m}}^{+\infty}\frac{d\omega'}{\pi}\frac{\mathrm{Im}[\chi_{xx}(\omega')]}{\omega'-\omega} + \sum_{j=1}^{m-1}\int_{\omega_{2j}}^{\omega_{2j+1}}\frac{d\omega'}{\pi}\frac{\mathrm{Im}[\chi_{xx}(\omega')]}{\omega'-\omega}, & \text{otherwise,}\end{cases}\end{aligned} \tag{24}$$

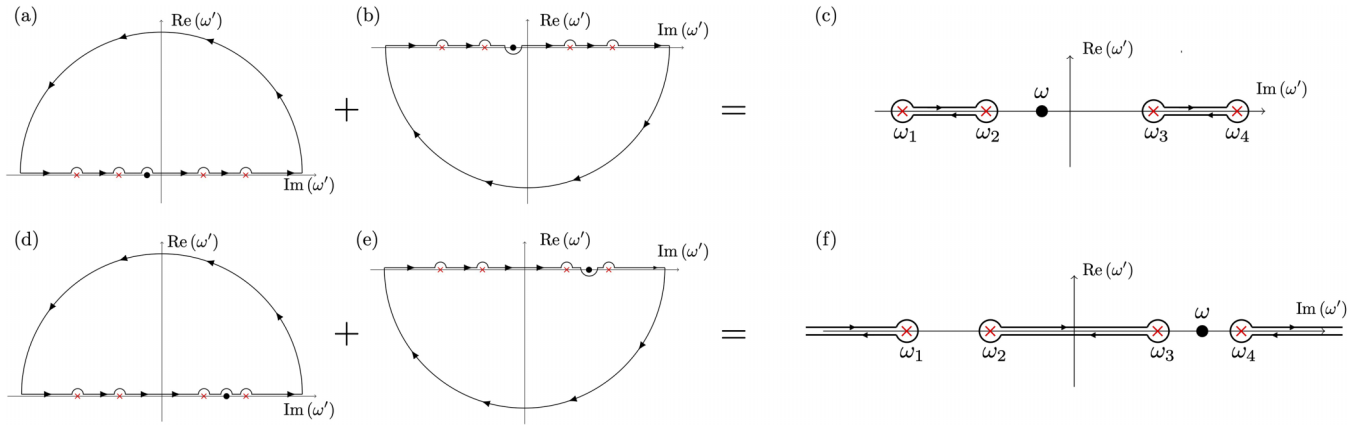

FIG. 1. Integration contours that schematically show how to evaluate the principal values in Eqs. (24) and (25), depending on the position of the pole $\omega' = \omega$. When the point $\omega' = \omega$ has an even number of poles to its left, a series of finite branch cuts are made between neighboring branch points ω_j, and the sum of the integration contours, and panels (a) and (b) become a series of dogbone contours around the corresponding branch cuts, as depicted in panel (c). When ω instead has an odd number of poles to its left, the sum of the contours in (d) and (e) deform into two hairpin contours between $-\infty$ and the leftmost branch point, and the rightmost branch point to $+\infty$, denoted ω_1 and ω_4 in (f), respectively, and a sum of finite dogbone contours between the rest of neighboring branch points, as depicted in panel (f).

$$-\mathrm{Im}[\chi_{xy}(\omega)] = \mathrm{PV}\int_{-\infty}^{\infty}\frac{d\omega'}{\pi}\frac{\mathrm{Re}[\chi_{xy}(\omega')]}{\omega'-\omega}$$
$$= \begin{cases} \sum_{j=1}^{m}\int_{\omega_{2j-1}}^{\omega_{2j}}\frac{d\omega'}{\pi}\frac{\mathrm{Re}[\chi_{xy}(\omega')]}{\omega'-\omega}, & \omega \text{ has even number of poles to the left} \\ \int_{-\infty}^{\omega_1}\frac{d\omega'}{\pi}\frac{\mathrm{Re}[\chi_{xy}(\omega')]}{\omega'-\omega} + \int_{\omega_{2m}}^{+\infty}\frac{d\omega'}{\pi}\frac{\mathrm{Re}[\chi_{xy}(\omega')]}{\omega'-\omega} + \sum_{j=1}^{m-1}\int_{\omega_{2j}}^{\omega_{2j+1}}\frac{d\omega'}{\pi}\frac{\mathrm{Re}[\chi_{xy}(\omega')]}{\omega'-\omega}, & \text{otherwise.} \end{cases} \quad (25)$$

which is the central result of this section.

It should be strongly emphasized that the expressions Eqs. (24) and (25) hold true for *any* continuously differentiable functions $h(k_z)$ and $g(k_z)$. Due to the general nature of these expressions, performing the integrals or the sums explicitly and arriving at a more compact final result will not be possible unless the specific model under consideration is specified. In fact, leaving the expressions as they currently stand actually makes it possible to predict the generic behavior of, e.g., the magneto-optical Hall conductivity for Weyl semimetals. For example, the changes of branch cuts when sweeping through ω space will manifest as an abrupt transition in the conductivity spectrum, e.g., as sharply approaching a positive (negative) value, suddenly transitioning to the corresponding negative (positive) value, and then starting to increase again; a behavior that could be intuitively thought of as a mirroring in a straight line passing through the corresponding branch point. Hence, these expressions will be left as they stand.

D. dc limit

The expressions derived above are only valid for nonzero frequencies, meaning that the dc limit ($\omega \to 0$) has to be studied separately. In terms of the response function, this has to be done with caution as the order of various limits and integrations do not necessarily commute. Recalling the Kubo formula, the conductivity reads in the dc limit reads

$$\sigma_{\mu\nu}(0) = \lim_{\omega\to 0}\left\{\frac{1}{i\omega}[\chi_{\mu\nu}(\omega) - \chi_{\mu\nu}(0)]\right\} = \frac{1}{i}\frac{d}{d\omega}\chi_{\mu\nu}(\omega)_{|_{\omega=0}}. \quad (26)$$

Instead of carrying out this derivative, we here choose to employ the Kramers-Kronig relations once again, and illustrate how these can be used to arrive at an analytical closed-form expression for the dc Hall conductivity. This reads

$$\mathrm{Re}[\sigma_{xy}(0)] = \lim_{\omega\to 0}\frac{1}{\omega}\{\mathrm{Im}[\chi_{xy}(\omega)] - \mathrm{Im}[\chi_{xy}(0)]\}$$
$$= \lim_{\omega\to 0}\mathrm{PV}\int_{-\infty}^{+\infty}\frac{d\omega'}{\pi}\frac{\mathrm{Re}[\chi_{xy}(\omega')]}{\omega'(\omega'-\omega)}. \quad (27)$$

Before formally taking the limit, we need to make sure this can be done in a consistent way with respect to the choice of branch cuts. For this, we assume that ω is very small, so there exists no branch points between $\omega' = 0$ and $\omega' = \omega$. This corresponds to case 1 in Sec. II C, and thus the dc Hall conductivity reads

$$\mathrm{Re}[\sigma_{xy}(0)] = -\lim_{\omega\to 0}\sum_{j=1}^{m}\int_{\omega_{2j-1}}^{\omega_{2j}}\frac{d\omega'}{\pi}\frac{\mathrm{Re}[\chi_{xy}(\omega')]}{\omega'(\omega'-\omega)}. \quad (28)$$

If the limit $\omega \to 0$ is now naively taken before the integration is performed, the pole at $\omega' = 0$ will become a pole of order 2 instead of order 1. Consequently, the integration along the small semicircular contours around $\omega' = 0$ will not vanish, but rather result in divergences which do not necessarily cancel

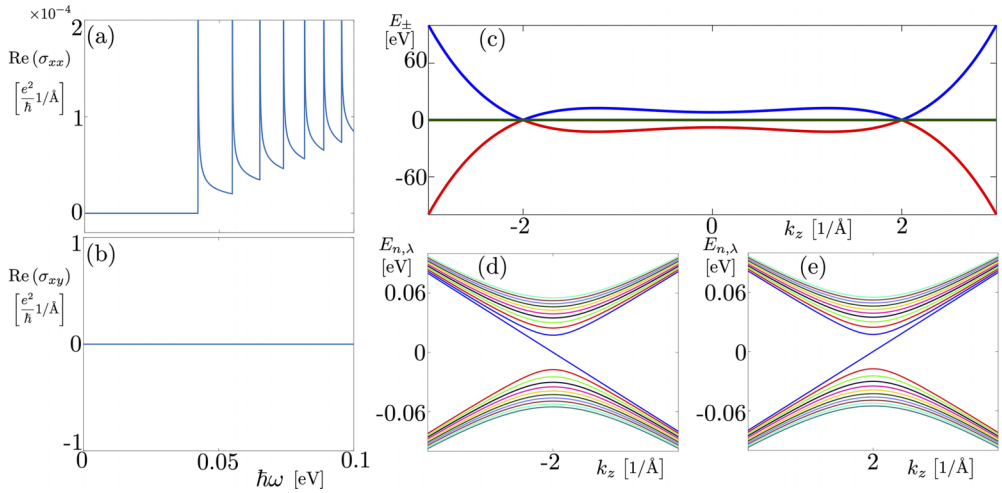

FIG. 2. Real parts of $\sigma_{xx}(\omega)$ (a) and $\sigma_{xy}(\omega)$ (b) for parameter values $\alpha = 2$, $\beta = 1$, $\gamma = 2$, $\eta_+ = \eta_- = 0$, $\mu = 0\,\text{eV}$, and $B = 10\,\text{T}$. The band structure in the absence of a magnetic field is shown in (c), while (d) and (e) show the Landau level structure at $k_z = \pm\alpha$. The peak structure in σ_{xx} is also kept when two nodes are considered and corresponds to interband transitions between Landau levels from the conduction to the valence band, but the contribution from the transition between the chiral level and the first Landau level is canceled. This is because there will be exactly opposite contributions from the two nodes, one from the chiral level to the first Landau level at one node, and the reversed transition at the second node. Since there are no Fermi pockets, there are no allowed intraband transitions, causing σ_{xy} to be vanishing for all ω.

each other. Therefore, this is as far as the analytical simplifications go, and we will use Eq. (28) to evaluate the Hall conductivity in the dc-limit.

III. MAGNETO-OPTICAL CONDUCTIVITY FOR SYMMETRICALLY SPACED WEYL NODES

We now turn to apply the techniques developed above for concrete setups. We will use a model whose dispersion is given by

$$g(k_z) := \gamma\left(k_z^2 - \alpha^2\right)\left(k_z^2 + \beta^2\right), \tag{29}$$

$$h(k_z) := ak_z^4 + bk_z^3 + ck_z^2 + dk_z + e, \tag{30}$$

where all the constants are real. Such a system has a pair of Weyl nodes symmetrically separated in momentum at $k_z = \pm\alpha$. Both $g(k_z)$ and $h(k_z)$ are taken to be fourth order, and the parameters can be tuned such that potential Fermi pockets in connection to the nodes will be kept finite in size. The coefficients of $h(k_z)$ will be defined through

$$h(\pm\alpha) = E_{\mathrm{W}_\pm}, \quad h'(\pm\alpha) = \eta_\pm, \tag{31}$$

where $E_{\mathrm{W}_\pm}$ denote the energy at the Weyl node at $k_z = \pm\alpha$, and $\eta_\pm$ controls the tilt at $k_z = \pm\alpha$. Manually setting a to assure finite Fermi pockets, and $E_{\mathrm{W}_\pm} = 0$, the coefficients of $h(k_z)$ are defined as

$$a = 0.01, \tag{32}$$

$$b = \frac{\eta_+ + \eta_-}{4\alpha^2}, \tag{33}$$

$$c = \frac{-2b\alpha^2 - 4\alpha^3 + \eta_+}{2\alpha}, \tag{34}$$

$$d = -b\alpha^2, \tag{35}$$

$$e = -d\alpha - c\alpha^2 - b\alpha^3 - a\alpha^4. \tag{36}$$

Initially, we will investigate how the conductivity behaves when varying the tilt parameters. For the sake of clarity, we will treat different kinds of systems in separate subsections. We will focus on the real parts of σ_{xx} and σ_{xy} for the results, i.e., we will display one dissipative and one reactive component of the response function.

A. Untilted and tilted type I

Let us start with a system where both nodes are untilted, i.e., where $\eta_+ = \eta_- = 0$. The real parts of σ_{xx} and σ_{xy} are displayed in Figs. 2(a) and 2(b), respectively, where the xx component displays the characteristic peak structure, corresponding to optical interband Landau-level transitions of neighboring indices, i.e., the nth Landau level with $\lambda = -1$ transition to the $(n+1)$th Landau level with $\lambda = +1$, as thoroughly explained in Refs. [30–33]. The position of the peaks correspond exactly to the difference in energy between respective Landau-level pairs, which agrees with previous studies where typically systems hosting only one Weyl node are studied. An important difference here, however, is that the contribution from the transition from the chiral level is absent. This is seen as a small bump located at the energy corresponding to the difference between the chiral level and the first Landau level at the Weyl node, cf. Refs. [30–33]. Here, however, we have matching, but opposite, contributions from the two nodes, which makes the net contribution vanish. As $\mu = 0$ in Fig. 2, the Hall conductivity vanishes for all ω and provides nothing interesting at this stage.

In Fig. 3, the dispersion around one of the nodes have been tilted slightly, while the other is kept untilted. As the tilt is weak enough to ensure that neither the valence band nor the conduction band cross, but merely touch, the Fermi level at the Weyl nodes, there are no additional transitions that can occur. Therefore, the result in this case very much resembles that of

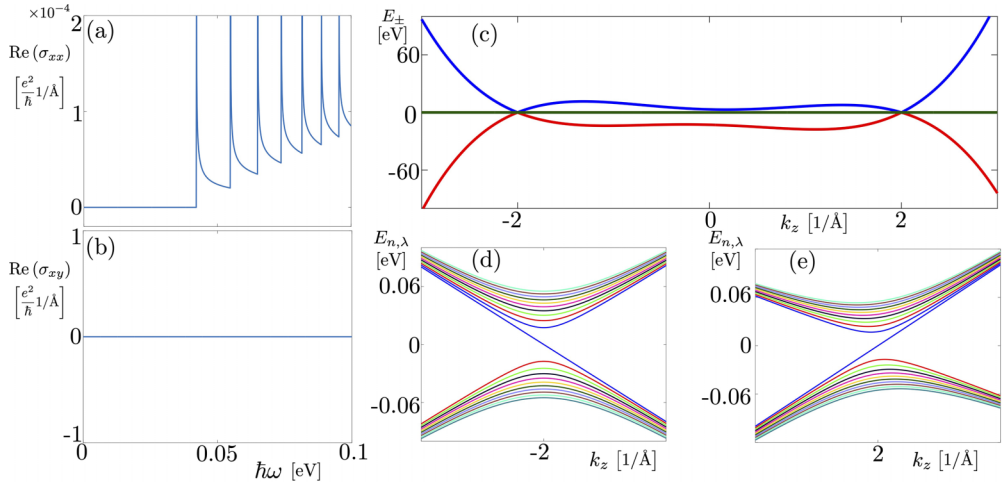

FIG. 3. Real parts of $\sigma_{xx}(\omega)$ (a) and $\sigma_{xy}(\omega)$ (b) for parameter values $\alpha = 2$, $\beta = 1$, $\gamma = 2$, $\eta_+ = 10$, $\eta_- = 0$, $\mu = 0\,\text{eV}$, and $B = 10\,\text{T}$. The band structure in the absence of a magnetic field is shown in (c), while (d) and (e) show the Landau-level structure at $k_z = \pm\alpha$. The weak tilting of the node at $k_z = 2$ leaves the behavior of both σ_{xx} and σ_{xy} unchanged, which is a consequence from there still being no allowed intraband transitions.

two untilted nodes; the xx component still has its characteristic peaks, while the xy component remains vanishing.

B. Tilted type II

When the tilt is increased further, the valence and/or conduction band may fully cross the Fermi level, and the Weyl semimetal enters the type-II-phase. This phase is distinguished from the type-I phase by that the Fermi surface becomes finite and thus is no longer pointlike. In the context of conductivity, this allows for intraband transitions, i.e., transitions between neighboring Landau levels with the same value of λ. Just as for the interband transitions, they appear at energies corresponding exactly to the energy difference of the respective Landau level pairs, which in this case are spaced much closer together. This can be seen in Fig. 4, where one of the nodes is kept untilted and the other is tilted such that the Fermi pockets are formed, cf. Figs. 4(c)–4(e). In addition to the interband peaks, the intraband peaks are located close to $\hbar\omega = 0$. Notably, the type-II phase also hosts a nontrivial Hall conductivity σ_{xy}, which can be seen in Fig. 4(b).

When just slightly tilting the previously untilted node, nothing interesting initially happens (cf. Fig. 5), but when the second node is eventually overtilted as well, the behavior of

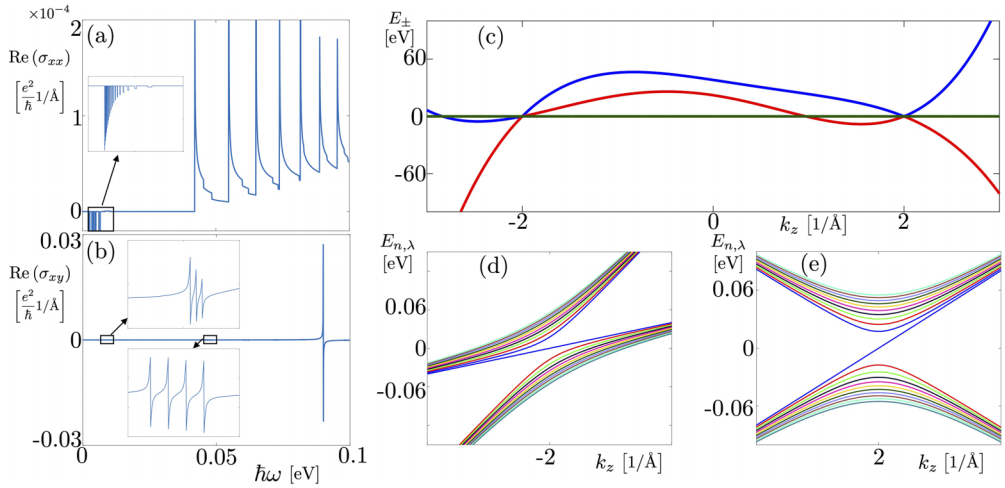

FIG. 4. Real parts of $\sigma_{xx}(\omega)$ (a) and $\sigma_{xy}(\omega)$ (b) for parameter values $\alpha = 2$, $\beta = 1$, $\gamma = 2$, $\eta_+ = 0$, $\eta_- = 60$, $\mu = 0\text{eV}$ and $B = 10\text{T}$. The band structure in the absence of a magnetic field is shown in (c), while (d) and (e) show the Landau level structure at $k_z = \pm\alpha$. As a consequence of the existence of Fermi pockets, intraband transitions are allowed, which gives a response at smaller frequencies. Additionally, there are interband transitions happening at non-zero k_z, which can be seen as the small steps between the peaks in panel (a). These transitions do not happen in a symmetric fashion, since the Fermi pockets are only present in direct connection to the tilted node. This gives a response also in the Hall conductivity, which is seen as sharp transitions in panel (b). Mathematically, these correspond exactly to at what frequencies the choices of branch cuts, and hence integration contours, are changed, making it possible to interpret the Hall response as a branch point transition, agreeing with the interpretation of Eqs. (24) and (25).

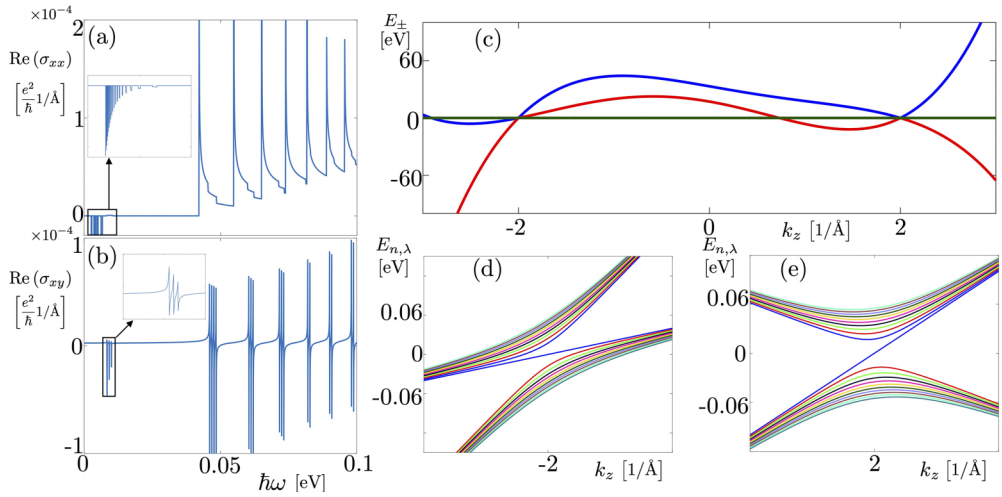

FIG. 5. Real parts of $\sigma_{xx}(\omega)$ (a) and $\sigma_{xy}(\omega)$ (b) for parameter values $\alpha = 2$, $\beta = 1$, $\gamma = 2$, $\eta_+ = 10$, $\eta_- = 60$, $\mu = 0\,\text{eV}$ and $B = 10\,\text{T}$. The band structure in the absence of a magnetic field is shown in (c), while (d) and (e) show the Landau level structure at $k_z = \pm\alpha$. The weak tilting of the node located at $k_z = 2$ does not affect the result significantly from the case where this node is untilted (cf. Fig. 4).The peak structure in (a) behaves similarly, and we see essentially equivalent behavior of the Hall conductivity in (b), even though it seems as if the strength of the response is more even throughout the considered energy spectrum. This could, however, just be a consequence of the evaluation of the principal value—the size of the peaks are not to be taken literal.

the conductivity changes significantly. Notably, the Hall conductivity becomes highly oscillating along all energies shown in Fig. 6, while the *xx* component is left somewhat unchanged, with the important exception being a slight deviation from 0 at the same frequencies as the oscillatory behavior of σ_{xy} begins. This behavior is caused by the existence of two particle-hole pairs of Fermi pockets, vastly increasing the number of allowed Landau-level transitions.

C. Trivial pockets

Another interesting phenomena that might be present in Weyl semimetals is trivial Fermi pockets. These are formed when either the valence or conduction band cross the Fermi energy away from a Weyl node. Consequently, the boundary of a trivial Fermi pocket does not contain the Weyl node, cf. Fig. 7(c), where the trivial Fermi pocket can be seen as the region where the red band attain positive energy values. The existence of trivial Fermi pockets also allows for intraband transitions, and these systems are therefore very much reminiscent of a type-II-system. In Fig. 7 we display the conductivity for such a system, which is created by tilting one of the nodes slightly, but not into the type-II regime. As a consequence of the existence of trivial Fermi pockets and the allowed intraband transitions, the conductivity very much behaves like that in a type-II system.

IV. DISCUSSION AND EXPERIMENTAL RELEVANCE OF RESULTS

The results in Sec. III show that studying systems with a chiral pair of Weyl nodes gives two important differences compared to those including only one node; the contribution from the transition to (from) the chiral level at the Weyl nodes exactly cancel each other, and the frequencies at which intraband transitions occur are smeared out. This claim is supported by comparing the systems studied in Sec. III to those studied in, e.g., Ref. [32], which display intraband contributions at significantly higher frequencies at similar field strengths. This serves as an indicator that additional nodes smear out the energy scale at which the intraband transitions are allowed, and that considering even more nodes could be a way to understand why the distinct peak structure sourced by interband transitions is not visible in experiments; if intraband and interband transitions occur at similar energy scales, the response from the intraband transitions will, due to their significantly larger response signal, mask that of the interband transitions and provide a possible explanation for the mismatch between theory and experiments. The absence of a clear chiral contribution is due to the fact that the energy splittings between the chiral level and the first Landau level are equal exactly at the Weyl nodes. It is important to note that this does not completely eliminate the contribution from the chiral level, since transitions away from the Weyl nodes may very well occur, but the strength of these are highly suppressed by competing transitions (cf. Fig. 6). The individual signatures from both intraband and interband transitions, however, remain intact when higher-order terms of momentum and additional Weyl nodes are considered, which indicate that to study these phenomena separately, systems hosting only one Weyl node will suffice. What studies beyond single-node systems contribute is the important interplay between these signatures, which could serve as an explanation for the mismatch between theory and experiment. This is, of course, not the only such possible source, and we now turn to discuss some of them separately.

A. Beyond the clean limit

All the results presented in Sec. III display a very sharp peak structure, something that is not seen in experiments [34–36]. This structure is (theoretically) present regardless of

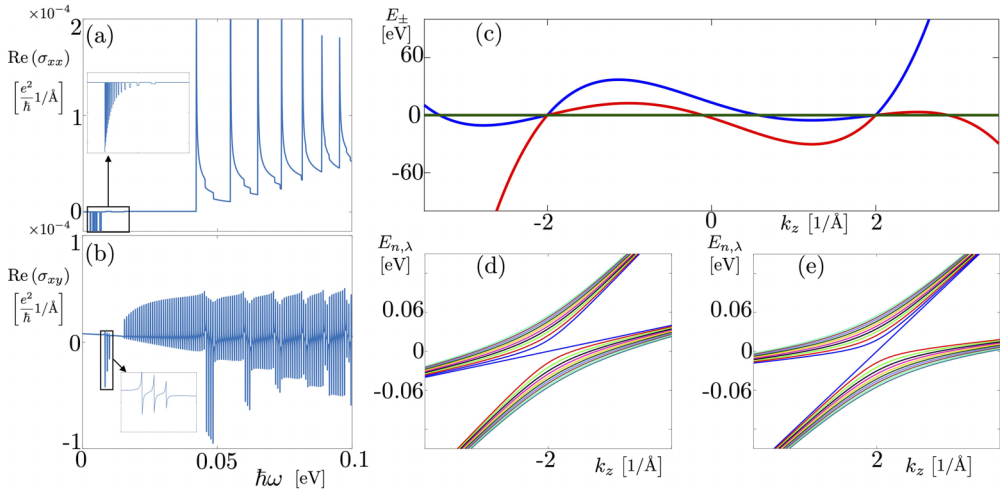

FIG. 6. Real parts of $\sigma_{xx}(\omega)$ (a) and $\sigma_{xy}(\omega)$ (b) for parameter values $\alpha = 2$, $\beta = 1$, $\gamma = 2$, $\eta_+ = 50$, $\eta_- = 60$, $\mu = 0\,\text{eV}$, and $B = 10\,\text{T}$. The band structure in the absence of a magnetic field is shown in (c), while (d) and (e) show the Landau-level structure at $k_z = \pm\alpha$. The behavior of σ_{xx} seems to remain the same as in Fig. 5, but the response of the Hall conductivity has become highly oscillatory. Taking a closer look, σ_{xx} actually deviates slightly from 0 starting at the same frequency as the oscillations of σ_{xy}. These two features indicate that the number of allowed transitions vastly increases in this regime, which can be explained by the existence of two particle-hole pairs of Fermi pockets in the band structure (a).

if the approximation of the studied Weyl systems is linear [30,31], considers only one node [32,33], or, as shown in this paper, if a pair of nodes is considered. This particular mismatch is most likely a consequence of the theoretical studies being carried out in the clean limit, i.e., the regulator ϵ in Eq. (8) is taken to zero. A finite regulator can be thought of as assigning impurities or, more concretely, a finite scattering lifetime in the system [30]. This will slightly smear out the peaks and make the overall structure of the conductivity smoother, and hence it should be emphasized that the impact of a finite impurity scattering lifetime is well understood as a concept on its own. Consequently, we do not expect any remarkable differences in the conductivity spectrum going beyond the clean limit, which is why the features observed and conclusions made in the current paper will hold also when including impurity scattering, which in turn increases the credibility of the results. Numerical simulations beyond the clean limit are therefore beyond the current scope and the exact impact of impurity scattering is left for future studies.

B. Symmetry-breaking and nodes at different energies

In this paper, we have restricted ourselves to present plots of systems where the Weyl nodes are spaced symmetrically in momentum space and where they both appear at zero energy. It should be noted that the general reasoning, and hence the expressions for the linear response function, is applicable to any general polynomials $g(k_z)$ and $h(k_z)$, and that the

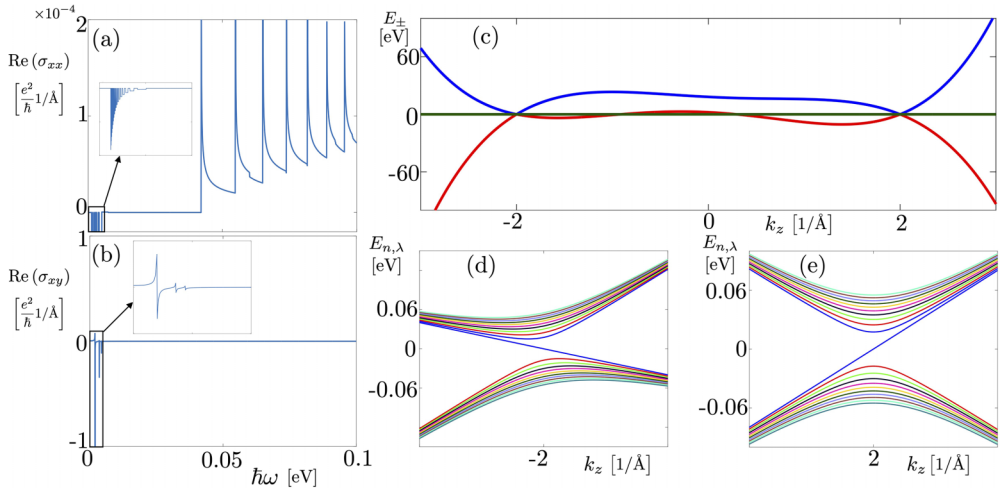

FIG. 7. Real parts of $\sigma_{xx}(\omega)$ (a) and $\sigma_{xy}(\omega)$ (b) for parameter values $\alpha = 2$, $\beta = 1$, $\gamma = 2$, $\eta_+ = 0$, $\eta_- = 20$, $\mu = 0\,\text{eV}$, and $B = 10\,\text{T}$. The band structure in the absence of a magnetic field is shown in (c), while (d) and (e) show the Landau-level structure at $k_z = \pm\alpha$. The presence of trivial Fermi pockets results in a response similar to those features observed in type-II systems, which is a consequence of intraband transitions being allowed. This results in a Hall response (b) and a sharp contribution for very low frequencies for the xx component (a).

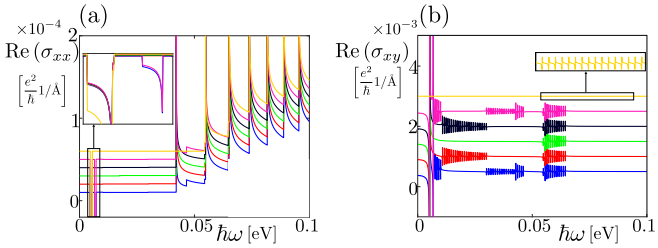

FIG. 8. Real parts of $\sigma_{xx}(\omega)$ (a) and $\sigma_{xy}(\omega)$ (b) for parameter values $\alpha = 2$, $\beta = 1$, $\gamma = 2$, $\eta_+ = 0$, $\eta_- = 20$, $\mu = 0.03\,\text{eV}$, and $B = 10\,\text{T}$ for different locations in energy of the Weyl node at $k_z = -\alpha$. Blue, red, green, black, magenta, and yellow correspond to $E(-\alpha) = 0.01, 0.02, 0.03, 0.04, 0.05$, and $0.06\,\text{eV}$, respectively. The results for such different energies are shifted in steps of 10^{-5} in (a) and 2×10^{-4} in (b) to allow reasonable visibility. The conductivity properties change qualitatively with the energy difference between the nodes, as it allows for some additional transitions, and forbids some that were previously allowed. For instance, the first interband transition for $E(-\alpha) = 0.06\,\text{eV}$ is not the same as for the other values of $E(-\alpha)$, which can be seen in (a) as the first peak of the yellow curve coincides with the second peak of the other curves. Having a nonzero energy difference between the nodes also gives a Hall response, seen in (b), but this time as a consequence of allowed intraband and interband transitions. The former further gives a sharp response at lower frequencies in (a).

restriction is only in terms of the displayed plots. However, as the behavior of both σ_{xx} and σ_{xy} can be thoroughly understood in terms of Landau-level transitions, this restriction can be made almost without loss of any generality. This can be understood as follows.

Consider first the case where the nodes are symmetrically spaced in momentum. Regardless of at what momenta they are located, the Landau levels at the Weyl nodes will be equally split in energy—this splitting does not depend on the position of the nodes in momentum space but rather by the magnetic field [recall that they appear exactly when $g(k_z) = 0$]. The position of the nodes might, however, affect the Landau-level splitting at the points where the intraband transition occurs, as these generically happen at momenta where $g(k_z)$ is nonzero. But this is also the case for symmetrically spaced nodes, as the tilt at the respective nodes will source similar features in the Landau-level splitting. Hence, breaking this symmetry is not expected to give rise to any new physics but rather will change the location of the intraband transitions in a way similar to what the tilting at the respective nodes does.

Now, what would happen if the nodes appear at different energies? Again, this will not change the Landau-level splitting at the nodes, but it will change the allowed transitions and break the symmetry between the transitions among the nodes. This would allow for contributions from interband transitions to the Hall conductivity, illustrated in Fig. 8, along with the more conventional contributions from intraband transitions. Thus, it can be concluded that the location of the nodes in energy space is reflected in the optical response.

C. dc limit

Albeit the analytical tools used in this paper are not ideal in terms of stability for investigating the dc limit, we will devote this subsection to understanding the dc Hall conductivity as a function of various system parameters. But before evaluating Eq. (28) explicitly, let us think about what conclusions can be made from the expression itself, highlighting the strength of analytical frameworks when it comes to phenomenological understanding. We know that optical Landau level transitions are what contributes to the optical Hall conductivity, which due to the Kramers-Kronig relations, Eqs. (22) and (23), are also what will contribute in the dc limit. This means that we should observe a stepwise change in the dc conductivity when changing the chemical potential, since this will control the number of allowed transitions. When μ sweeps through an additional Landau level, the curve will change shapes. However, it does not necessarily mean that we expect a clean plateau structure, not even in the $T \to 0$-limit, even though the Fermi functions become step functions. Instead, the effect is that the integration domain is extended, and therefore the dc Hall conductivity should consist of a series of glued, piecewise smooth functions. This is exactly what is observed in Ref. [41]. Interestingly enough, the authors of Ref. [41] understood this behavior in terms of the density of states, while our reasoning connects the same phenomena to Landau-level transitions and choices of branch cuts. We include a plot of the dc Hall conductivity as a function of μ in Fig. 9(a), obtained from evaluating Eq. (28).

The chemical potential is not alone responsible for controlling which intraband transitions are allowed. The tilts at the different nodes have a similar effect, meaning that the piecewise structure should also be observed as a function of η_+ and η_- in Eqs. (32) and (33). This is indeed what we see in Fig. 9(b). That the tilt has significant impact on the Hall conductivity is something that is also mentioned in Ref. [41], even though they merely considered a couple of different tilting values.

Another feature of the Hall conductivity is its relation to the spacing between the Weyl nodes. From field theoretical techniques, it is predicted that the current related to the Hall conductivity is proportional to this distance (in momentum space) in the presence of an electric field [13]. On a similar note, we here investigate how the distance in momentum space between the nodes affect the dc Hall response in Weyl semimetals when subject to a constant magnetic field. This is shown in Fig. 9(c), from which we can conclude that the distance plays a significant role in the Hall response, but the scaling between the two quantities is not very direct. In fact, it takes a rational polynomial in the form $\sigma_{xy}^{\text{dc}}(\alpha) = \frac{c_1}{\alpha^3 + c_2\alpha^2 + c_3\alpha + c_4}$, with $(c_1, c_2, c_3, c_4) = 10^3 \times (0.0224, 0.2516, 1.7408, -1.9876)$ to fit the data reasonably, cf. Fig. 9(c).

D. Finite temperature

As all the general and illustrated results are carried out in the limit of zero temperature, the effect of going to finite temperature must be mentioned. We will exclusively focus on the temperature dependence of the Hall conductivity, as it has previously been noted that the peak structure in the σ_{xx} component is not notably affected at finite temperatures [32]. For the Hall conductivity, going to finite temperature will result in additional Matsubara poles in the lower half complex

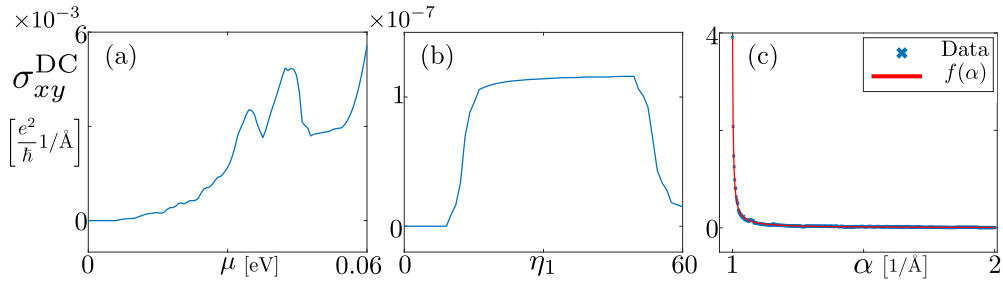

FIG. 9. dc Hall conductivity as a function of chemical potential μ (a), tilting at the node at $k_z = \alpha$ (b), and the splitting between the nodes (c) for $\alpha = 2$ (a), (b); $\beta = 1$, $\gamma = 2$, $\eta_+ = 0$, $\eta_- = 20$ (a), (c); $\mu = 0.03\,\mathrm{eV}$ (b), (c); and $B = 10\,\mathrm{T}$. Albeit being an unstable expression, Eq. (28) captures the gluing features predicted for (a) and (b), i.e., that the Hall conductivity should consist of piecewise smooth functions of chemical momentum or tilt. In (c), it becomes apparent that the distance between the Weyl nodes is highly relevant for the strength of the response signal. As a function of the location of the respective Weyl nodes, the conductivity can be approximated as $\sigma^{\mathrm{dc}}_{xy}(\alpha) = \frac{c_1}{\alpha^3 + c_2\alpha^2 + c_3\alpha + c_4}$, with $(c_1, c_2, c_3, c_4) = 10^3 \times (0.0224, 0.2516, 1.7408, -1.9876)$.

ω plane. These will be at values of ω, satisfying

$$\frac{E_{n,\lambda}(k_i) - \mu}{k_B T} = i\pi(2m - 1), \tag{37}$$

where $m \leqslant 0$ to maintain the analytical properties of the response function in the upper half complex ω plane. Thus, in addition to retaining the original prefactors $A_n^{\lambda\lambda'}(k_i)$ in terms of the Fermi distribution functions, there will be contributions on the form

$$2\pi i \sum_j \mathrm{Res}\{\mathrm{Re}[\chi_{xy}(\omega)], \omega_j\}, \tag{38}$$

where ω_j solves Eq. (37). These corrections are not treatable using the analytical tools developed in this paper, and hence lie beyond the current scope. Their complete contribution amounts to an infinite sum, the convergence and decay of which has to be properly investigated to assert a termination of the sum to a finite one to be motivated. In the dc limit, and assuming a convergent thermal contribution, one could guess the impact of these corrections. As a function of chemical potential, or tilting parameters, the piecewise gluing of curves is expected to be smoothed out when the Fermi functions are reintroduced. For low temperatures, the impact of the Matsubara poles can be further understood, in general, from the results of Ref. [32]. Comparing the small stairlike steps located in between the sharp peaks in Figs. 5(a), 6(a), and 7(a), which is sourced by intraband transitions exclusively related to the existence of Fermi pockets, with those appearing at finite temperature in similar systems in, e.g., Fig. 3(a) of Ref. [32], those at finite temperature are smoother compared to those at zero temperature. In terms of the Hall response, this will smooth out the sharp transition structure seen in Figs. 5(b), 6(b), and 7(b). However, since the temperature studied in Ref. [32] (which was set to 5 K) shows a minor impact on the final result, and that this impact is further well understood, we do not expect any significant changes as long as the temperatures are kept low. For increasing temperatures, however, these might have a more profound effect that should be investigated in future works.

It should lastly be emphasized that the Kramers-Kronig relations rely on causality, which is what causes the response function to be analytical in the upper half complex ω-plane. When considering systems at finite temperature, thus going beyond the zero-temperature limit, the very notion of causality becomes affected, which in turn alters the Kramers-Kronig relations. Since the general method calculating the Hall conductivity developed in this paper is based exactly on the Kramers-Kronig relations, it is not unexpected that things become complicated when thermal effects are taken into account. Exactly how complicated this becomes, and how profound the effects are, is left as an open question to be answered in subsequent studies.

V. SUMMARY OF RESULTS AND OUTLOOK

In this paper, we have expanded on the analytical and general theory calculating magneto-optical conductivity in Weyl semimetals. To complement previous works where the dissipative components of the linear response function have been computed, we here also provide analytical closed-form expressions for the reactive components in terms of a sum of finite integrals (and potentially semi-infinite integrals). This allows for the analytical calculation of the optical Hall conductivity beyond the high-field quantum- or dc limit for generic Weyl semimetals, and for understanding physical features directly by studying the corresponding band structure in combination with the analytical expressions. The theoretical and abstract calculations are then applied to a Weyl system hosting two nodes with potential tilts, which further extends previous works where systems hosting only one node are typically considered. Importantly, the simulation includes systems where fourth-order momentum terms are taken into account to make sure that potential Fermi pockets are finite in size. This allows us to study magneto-optical transport, in principle, including contributions from all Landau levels as a function of tilting at both nodes, Weyl node splitting in momentum space, and chemical potential, without the need of unphysical cutoffs in momentum or energy. Apart from the ac optical conductivity, a closed-form expression for the dc limit of the Hall conductivity is also derived, from which phenomenological conclusions matching with existing literature are made.

Our paper has further verified that neither higher-order corrections in momentum nor the existence of additional Weyl nodes changes individual signatures of the magneto-optical spectrum significantly—the individual features linked to interband and intraband transitions seen in the simulations in

this paper can also be studied in simpler systems hosting only one node. There are, however, two important deviations, the first being the absence of a contribution from a transition involving the chiral Landau level, as opposite transitions occur at charge-conjugate Weyl nodes. The second, and more important, deviation, is that the relative energy range at which the intraband transition occurs seems to be significantly larger in systems with two nodes than in those with only one node. This further strengthens the hypothesis that these transitions, which come with a significantly larger response signal, are the main reason for the predicted sharp peak structure sourced by interband transitions to be masked in experiments; if intraband transitions are allowed at the same energy scales as interband transitions, the signal from the intraband transition will dominate. The general tools developed in this and previous works [32,33] can, in principle, be used to scan through various models and continue the search for the source of this mismatch.

In summary, our key findings are:

(1) the derivation of an analytical closed-form expression for the reactive components of the conductivity tensor, which allows for qualitative predictions of the magneto-optical response to be done directly from the band structure of candidate materials;

(2) the discovery that the contribution from the chiral level cancels between the different nodes; and

(3) the conclusion that considering a chiral pair of nodes smears out the energy range allowing for intraband transitions, strengthening the hypothesis that these are the source to the mismatch between theoretical predictions and experimental observations.

A natural extension of this paper would be to generalize the calculational tools to include higher-order Weyl nodes, which in recent works have shown to impact the tilt structure in the optical response [33]. Additional straightforward, yet involved, continuations include the finite-temperature picture, the impact of the Matsubara poles in Weyl systems, and the corresponding Hall conductivity. Lastly, a concrete direction towards finding the source of the mismatch between theory and experiment would be to use the developed analytical techniques for more realistic band structures of actual materials and to include interaction effects beyond linear response. This would require a combination of experimental measurement techniques, such as ARPES, and first-principles calculations, such as DFT, and comprising a promising path towards unifying experimental observations and theoretical predictions.

ACKNOWLEDGMENTS

We thank the group of Prof. A. Black-Schaffer, especially P. Holmvall and R. Arouca, for discussions and feedback on the results and on the project in general. We also thank Prof. T. Hans Hansson, Prof. E. J. Bergholtz, and Prof. J. Knolle for discussions and useful comments on the paper.

APPENDIX: RESPONSE FUNCTION FOR WEYL SEMIMETALS

1. Simplifications in the $T \to 0$ limit

Take as a starting point Eqs. (A26) and (A27) in Ref. [32], which state that

$$\begin{aligned}
\mathrm{Im}[\chi_{xx}(\omega)] = &-\frac{e^2 v_F^2}{16\pi l_B^2}\sum_{n=0}^{n_{\max}}\sum_{i=1}^{2m} \\
&\times\Bigg\{A_n^{++}(k_i)\Bigg[B_n^{+}(k_i)B_{n+1}^{-}(k_i)C_{n,n+1}^{++}(k_i)\theta(-\omega)\theta\left(\frac{2v_F^2}{l_B^2}-\omega^2\right) - B_n^{+}(k_i)B_{n+1}^{-}(k_i)C_{n+1,n}^{++}(k_i)\theta(\omega)\theta\left(\frac{2v_F^2}{l_B^2}-\omega^2\right)\Bigg] \\
&+A_n^{--}(k_i)\Bigg[B_n^{-}(k_i)B_{n+1}^{+}(k_i)C_{n,n+1}^{--}(k_i)\theta(\omega)\theta\left(\frac{2v_F^2}{l_B^2}-\omega^2\right) - B_n^{-}(k_i)B_{n+1}^{+}(k_i)C_{n+1,n}^{--}(k_i)\theta(-\omega)\theta\left(\frac{2v_F^2}{l_B^2}-\omega^2\right)\Bigg] \\
&+A_n^{+-}(k_i)\Bigg[B_n^{+}(k_i)B_{n+1}^{+}(k_i)C_{n,n+1}^{+-}(k_i)\theta(\omega)\theta\left(\omega^2-\frac{2v_F^2}{l_B^2}\right) - B_n^{+}(k_i)B_{n+1}^{+}(k_i)C_{n+1,n}^{-+}(k_i)\theta(-\omega)\theta\left(\omega^2-\frac{2v_F^2}{l_B^2}\right)\Bigg] \\
&+A_n^{-+}(k_i)\Bigg[B_n^{-}(k_i)B_{n+1}^{-}(k_i)C_{n,n+1}^{-+}(k_i)\theta(-\omega)\theta\left(\omega^2-\frac{2v_F^2}{l_B^2}\right) - B_n^{-}(k_i)B_{n+1}^{-}(k_i)C_{n+1,n}^{+-}(k_i)\theta(\omega)\theta\left(\omega^2-\frac{2v_F^2}{l_B^2}\right)\Bigg]\Bigg\},
\end{aligned} \tag{A1}$$

$$\begin{aligned}
\mathrm{Re}[\chi_{xy}(\omega)] = &-\frac{e^2 v_F^2}{16\pi l_B^2}\sum_{n=0}^{n_{\max}}\sum_{i=1}^{2m} \\
&\times\Bigg\{A_n^{++}(k_i)\Bigg[B_n^{+}(k_i)B_{n+1}^{-}(k_i)C_{n,n+1}^{++}(k_i)\theta(-\omega)\theta\left(\frac{2v_F^2}{l_B^2}-\omega^2\right) + B_n^{+}(k_i)B_{n+1}^{-}(k_i)C_{n+1,n}^{++}(k_i)\theta(\omega)\theta\left(\frac{2v_F^2}{l_B^2}-\omega^2\right)\Bigg] \\
&+A_n^{--}(k_i)\Bigg[B_n^{-}(k_i)B_{n+1}^{+}(k_i)C_{n,n+1}^{--}(k_i)\theta(\omega)\theta\left(\frac{2v_F^2}{l_B^2}-\omega^2\right) + B_n^{-}(k_i)B_{n+1}^{+}(k_i)C_{n+1,n}^{--}(k_i)\theta(-\omega)\theta\left(\frac{2v_F^2}{l_B^2}-\omega^2\right)\Bigg]
\end{aligned}$$

$$+A_n^{+-}(k_i)\left[B_n^{+}(k_i)B_{n+1}^{+}(k_i)C_{n,n+1}^{+-}(k_i)\theta(\omega)\theta\left(\omega^2-\frac{2v_F^2}{l_B^2}\right)+B_n^{+}(k_i)B_{n+1}^{+}(k_i)C_{n+1,n}^{-+}(k_i)\theta(-\omega)\theta\left(\omega^2-\frac{2v_F^2}{l_B^2}\right)\right]$$
$$+A_n^{-+}(k_i)\left[B_n^{-}(k_i)B_{n+1}^{-}(k_i)C_{n,n+1}^{-+}(k_i)\theta(-\omega)\theta\left(\omega^2-\frac{2v_F^2}{l_B^2}\right)+B_n^{-}(k_i)B_{n+1}^{-}(k_i)C_{n+1,n}^{+-}(k_i)\theta(\omega)\theta\left(\omega^2-\frac{2v_F^2}{l_B^2}\right)\right]\Bigg\}, \tag{A2}$$

with

$$A_n^{\pm\pm}(k_i):=f[E_{n,\pm}(k_i)]-f[E_{n+1,\pm}(k_i)]=\frac{\sinh\frac{E_{n+1,\pm}(k_i)-E_{n,\pm}(k_i)}{2k_BT}}{\cosh\frac{E_{n+1,\pm}(k_i)+E_{n,\pm}(k_i)-2\mu}{2k_BT}+\cosh\frac{E_{n+1,\pm}(k_i)-E_{n,\pm}(k_i)}{2k_BT}}, \tag{A3}$$

$$B_n^{\pm}(k_i):=1\pm\frac{g(k_i)}{\sqrt{g^2(k_i)+\frac{2n}{l_B^2}}}, \tag{A4}$$

$$C_{n,m}^{\pm\pm}(k_i):=\left|\frac{\hbar v_F\sqrt{g^2(k_i)+\frac{2n}{l_B^2}}\sqrt{g^2(k_i)+\frac{2m}{l_B^2}}}{g(k_i)g'(k_i)(E_{n,\pm}(k_i)-E_{m,\pm}(k_i))}\right|. \tag{A5}$$

Let us simplify this expression in the limit where $T\to 0$. In this limit, the A_ns become

$$A_n^{\lambda\lambda'}(k_i)\xrightarrow{T\to 0}\theta[\mu-E_{n,\lambda}(k_z)]-\theta[\mu-E_{n+1,\lambda'}(k_i)], \tag{A6}$$

which yield the following:

$$A_n^{++}(k_i)=\theta\left\{\mu-\hbar v_F\left[h(k_i)+\sqrt{\left(\frac{\omega}{2v_F}-\frac{v_F}{\omega l_B^2}\right)^2}\right]\right\}-\theta\left\{\mu-\hbar v_F\left[h(k_i)+\sqrt{\left(\frac{\omega}{2v_F}+\frac{v_F}{\omega l_B^2}\right)^2}\right]\right\}, \tag{A7}$$

$$A_n^{--}(k_i)=\theta\left\{\mu-\hbar v_F\left[h(k_i)-\sqrt{\left(\frac{\omega}{2v_F}-\frac{v_F}{\omega l_B^2}\right)^2}\right]\right\}-\theta\left\{\mu-\hbar v_F\left[h(k_i)-\sqrt{\left(\frac{\omega}{2v_F}+\frac{v_F}{\omega l_B^2}\right)^2}\right]\right\}, \tag{A8}$$

$$A_n^{+-}(k_i)=\theta\left\{\mu-\hbar v_F\left[h(k_i)+\sqrt{\left(\frac{\omega}{2v_F}-\frac{v_F}{\omega l_B^2}\right)^2}\right]\right\}-\theta\left\{\mu-\hbar v_F\left[h(k_i)-\sqrt{\left(\frac{\omega}{2v_F}+\frac{v_F}{\omega l_B^2}\right)^2}\right]\right\}, \tag{A9}$$

$$A_n^{-+}(k_i)=\theta\left\{\mu-\hbar v_F\left[h(k_i)-\sqrt{\left(\frac{\omega}{2v_F}-\frac{v_F}{\omega l_B^2}\right)^2}\right]\right\}-\theta\left\{\mu-\hbar v_F\left[h(k_i)+\sqrt{\left(\frac{\omega}{2v_F}+\frac{v_F}{\omega l_B^2}\right)^2}\right]\right\}. \tag{A10}$$

This means that these factors evaluate to

$$A_n^{++}(k_i)=\begin{cases}1, & \hbar v_F\left|\frac{v_F}{\omega l_B^2}-\frac{\omega}{2v_F}\right|<\mu-\hbar v_F h(k_i)<\hbar v_F\left|\frac{v_F}{\omega l_B^2}+\frac{\omega}{2v_F}\right|\\ 0, & \text{otherwise,}\end{cases} \tag{A11}$$

$$A_n^{--}(k_i)=\begin{cases}-1, & -\hbar v_F\left|\frac{v_F}{\omega l_B^2}+\frac{\omega}{2v_F}\right|<\mu-\hbar v_F h(k_i)<-\hbar v_F\left|\frac{v_F}{\omega l_B^2}-\frac{\omega}{2v_F}\right|\\ 0, & \text{otherwise,}\end{cases} \tag{A12}$$

$$A_n^{+-}(k_i)=\begin{cases}-1, & \hbar v_F\left|\frac{v_F}{\omega l_B^2}-\frac{\omega}{2v_F}\right|<\mu-\hbar v_F h(k_i)<-\hbar v_F\left|\frac{v_F}{\omega l_B^2}+\frac{\omega}{2v_F}\right|\\ 0, & \text{otherwise,}\end{cases} \tag{A13}$$

$$A_n^{-+}(k_i)=\begin{cases}1, & -\hbar v_F\left|\frac{v_F}{\omega l_B^2}-\frac{\omega}{2v_F}\right|<\mu-\hbar v_F h(k_i)<\hbar v_F\left|\frac{v_F}{\omega l_B^2}+\frac{\omega}{2v_F}\right|\\ 0, & \text{otherwise.}\end{cases} \tag{A14}$$

Also, the following simplifications can be done to the remaining factors of the response functions:

$$\begin{aligned}&B_n^{+}(k_i)B_{n+1}^{-}(k_i)C_{n,n+1}(k_i)\theta\left(\frac{2v_F^2}{l_B^2}-\omega^2\right)\\&=\left\{1-\frac{g^2(k_i)}{\frac{v_F^2}{\omega^2 l_B^4}-\frac{\omega^2}{4v_F^2}}+g(k_i)\left(\frac{1}{\left|\frac{v_F}{\omega l_B^2}-\frac{\omega}{2v_F}\right|}-\frac{1}{\left|\frac{v_F}{\omega l_B^2}+\frac{\omega}{2v_F}\right|}\right)\right\}\left|\frac{\frac{\omega^2}{4v_F^2}-\frac{v_F^2}{\omega^2 l_B^4}}{g(k_i)g'(k_i)\frac{\omega}{v_F}}\right|\theta\left(\frac{2v_F^2}{l_B^2}-\omega^2\right)\\&=\frac{\frac{2n+1}{l_B^2}-\frac{\omega^2}{2v_F^2}+\tilde{g}(k_i)}{\frac{v_F^2}{\omega^2 l_B^4}-\frac{\omega^2}{4v_F^2}}\left|\frac{\frac{\omega^2}{4v_F^2}-\frac{v_F^2}{\omega^2 l_B^4}}{g(k_i)g'(k_i)\frac{\omega}{v_F}}\right|\theta\left(\frac{2v_F^2}{l_B^2}-\omega^2\right)=\frac{\frac{2n+1}{l_B^2}-\frac{\omega^2}{2v_F^2}+\tilde{g}(k_i)}{|\tilde{g}(k_i)g'(k_i)|}\theta\left(\frac{2v_F^2}{l_B^2}-\omega^2\right),\end{aligned} \tag{A15}$$

$$
\begin{aligned}
&B_n^-(k_i)B_{n+1}^+(k_i)C_{n,n+1}(k_i)\theta\left(\frac{2v_F^2}{l_B^2}-\omega^2\right)\\
&\quad=\left\{1-\frac{g^2(k_i)}{\frac{v_F^2}{\omega^2 l_B^4}-\frac{\omega^2}{4v_F^2}}+g(k_i)\left(\frac{1}{\left|\frac{v_F}{\omega l_B^2}+\frac{\omega}{2v_F}\right|}-\frac{1}{\left|\frac{v_F}{\omega l_B^2}-\frac{\omega}{2v_F}\right|}\right)\right\}\left|\frac{\frac{\omega^2}{4v_F^2}-\frac{v_F^2}{\omega^2 l_B^4}}{g(k_i)g'(k_i)\frac{\omega}{v_F}}\right|\theta\left(\frac{2v_F^2}{l_B^2}-\omega^2\right)\\
&\quad=\frac{\frac{2n+1}{l_B^2}-\frac{\omega^2}{2v_F^2}-\tilde{g}(k_i)}{\frac{v_F^2}{\omega^2 l_B^4}-\frac{\omega^2}{4v_F^2}}\left|\frac{\frac{\omega^2}{4v_F^2}-\frac{v_F^2}{\omega^2 l_B^4}}{g(k_i)g'(k_i)\frac{\omega}{v_F}}\right|\theta\left(\frac{2v_F^2}{l_B^2}-\omega^2\right)=\frac{\frac{2n+1}{l_B^2}-\frac{\omega^2}{2v_F^2}-\tilde{g}(k_i)}{|\tilde{g}(k_i)g'(k_i)|}\theta\left(\frac{2v_F^2}{l_B^2}-\omega^2\right),
\end{aligned}
\tag{A16}
$$

$$
\begin{aligned}
&B_n^+(k_i)B_{n+1}^+(k_i)C_{n,n+1}(k_i)\theta\left(\omega^2-\frac{2v_F^2}{l_B^2}\right)\\
&\quad=\left\{1+\frac{g^2(k_i)}{\frac{\omega^2}{4v_F^2}-\frac{v_F^2}{\omega^2 l_B^4}}+g(k_i)\left(\frac{1}{\left|\frac{v_F}{\omega l_B^2}+\frac{\omega}{2v_F}\right|}+\frac{1}{\left|\frac{v_F}{\omega l_B^2}-\frac{\omega}{2v_F}\right|}\right)\right\}\left|\frac{\frac{\omega^2}{4v_F^2}-\frac{v_F^2}{\omega^2 l_B^4}}{g(k_i)g'(k_i)\frac{\omega}{v_F}}\right|\theta\left(\omega^2-\frac{2v_F^2}{l_B^2}\right)\\
&\quad=\frac{\frac{\omega^2}{2v_F^2}-\frac{2n+1}{l_B^2}+\tilde{g}(k_i)}{\frac{\omega^2}{4v_F^2}-\frac{v_F^2}{\omega^2 l_B^4}}\left|\frac{\frac{\omega^2}{4v_F^2}-\frac{v_F^2}{\omega^2 l_B^4}}{g(k_i)g'(k_i)\frac{\omega}{v_F}}\right|\theta\left(\omega^2-\frac{2v_F^2}{l_B^2}\right)=\frac{\frac{\omega^2}{2v_F^2}-\frac{2n+1}{l_B^2}+\tilde{g}(k_i)}{|\tilde{g}(k_i)g'(k_i)|}\theta\left(\omega^2-\frac{2v_F^2}{l_B^2}\right),
\end{aligned}
\tag{A17}
$$

$$
\begin{aligned}
&B_n^-(k_i)B_{n+1}^-(k_i)C_{n,n+1}(k_i)\theta\left(\omega^2-\frac{2v_F^2}{l_B^2}\right)\\
&\quad=\left\{1+\frac{g^2(k_i)}{\frac{\omega^2}{4v_F^2}-\frac{v_F^2}{\omega^2 l_B^4}}-g(k_i)\left(\frac{1}{\left|\frac{v_F}{\omega l_B^2}+\frac{\omega}{2v_F}\right|}+\frac{1}{\left|\frac{v_F}{\omega l_B^2}-\frac{\omega}{2v_F}\right|}\right)\right\}\left|\frac{\frac{\omega^2}{4v_F^2}-\frac{v_F^2}{\omega^2 l_B^4}}{g(k_i)g'(k_i)\frac{\omega}{v_F}}\right|\theta\left(\omega^2-\frac{2v_F^2}{l_B^2}\right)\\
&\quad=\frac{\frac{\omega^2}{2v_F^2}-\frac{2n+1}{l_B^2}-\tilde{g}(k_i)}{\frac{\omega^2}{4v_F^2}-\frac{v_F^2}{\omega^2 l_B^4}}\left|\frac{\frac{\omega^2}{4v_F^2}-\frac{v_F^2}{\omega^2 l_B^4}}{g(k_i)g'(k_i)\frac{\omega}{v_F}}\right|\theta\left(\omega^2-\frac{2v_F^2}{l_B^2}\right)=\frac{\frac{\omega^2}{2v_F^2}-\frac{2n+1}{l_B^2}-\tilde{g}(k_i)}{|\tilde{g}(k_i)g'(k_i)|}\theta\left(\omega^2-\frac{2v_F^2}{l_B^2}\right),
\end{aligned}
\tag{A18}
$$

with $\tilde{g}(k_i) := |\frac{\omega}{v_F}|g(k_i)$. Then, we arrive at

$$
\begin{aligned}
\mathrm{Im}[\chi_{xx}(\omega)] = &-\frac{e^2v_F^2}{16\pi l_B^2}\sum_{n=0}^{n_{\max}}\sum_{i=1}^{2m}\left\{A_n^{++}(k_i)\left[\frac{\frac{2n+1}{l_B^2}-\frac{\omega^2}{2v_F^2}+\tilde{g}(k_i)}{|\tilde{g}(k_i)g'(k_i)|}\right]\theta\left(\frac{2v_F^2}{l_B^2}-\omega^2\right)\mathrm{sgn}(-\omega)\right.\\
&+A_n^{--}(k_i)\left[\frac{\frac{2n+1}{l_B^2}-\frac{\omega^2}{2v_F^2}-\tilde{g}(k_i)}{|\tilde{g}(k_i)g'(k_i)|}\right]\theta\left(\frac{2v_F^2}{l_B^2}-\omega^2\right)\mathrm{sgn}(\omega)+A_n^{+-}(k_i)\left[\frac{\frac{\omega^2}{2v_F^2}-\frac{2n+1}{l_B^2}+\tilde{g}(k_i)}{|\tilde{g}(k_i)g'(k_i)|}\right]\theta\left(\omega^2-\frac{2v_F^2}{l_B^2}\right)\mathrm{sgn}(\omega)\\
&\left.+A_n^{-+}(k_i)\left[\frac{\frac{\omega^2}{2v_F^2}-\frac{2n+1}{l_B^2}-\tilde{g}(k_i)}{|\tilde{g}(k_i)g'(k_i)|}\right]\theta\left(\omega^2-\frac{2v_F^2}{l_B^2}\right)\mathrm{sgn}(-\omega)\right\},
\end{aligned}
\tag{A19}
$$

$$
\begin{aligned}
\mathrm{Re}[\chi_{xy}(\omega)] = &-\frac{e^2v_F^2}{16\pi l_B^2}\sum_{n=0}^{n_{\max}}\sum_{i=1}^{2m}\left\{A_n^{++}(k_i)\left[\frac{\frac{2n+1}{l_B^2}-\frac{\omega^2}{2v_F^2}+\tilde{g}(k_i)}{|\tilde{g}(k_i)g'(k_i)|}\right]\theta\left(\frac{2v_F^2}{l_B^2}-\omega^2\right)\right.\\
&+A_n^{--}(k_i)\left[\frac{\frac{2n+1}{l_B^2}-\frac{\omega^2}{2v_F^2}-\tilde{g}(k_i)}{|\tilde{g}(k_i)g'(k_i)|}\right]\theta\left(\frac{2v_F^2}{l_B^2}-\omega^2\right)+A_n^{+-}(k_i)\left[\frac{\frac{\omega^2}{2v_F^2}-\frac{2n+1}{l_B^2}+\tilde{g}(k_i)}{|\tilde{g}(k_i)g'(k_i)|}\right]\theta\left(\omega^2-\frac{2v_F^2}{l_B^2}\right)\\
&\left.+A_n^{-+}(k_i)\left[\frac{\frac{\omega^2}{2v_F^2}-\frac{2n+1}{l_B^2}-\tilde{g}(k_i)}{|\tilde{g}(k_i)g'(k_i)|}\right]\theta\left(\omega^2-\frac{2v_F^2}{l_B^2}\right)\right\}.
\end{aligned}
\tag{A20}
$$

2. Contribution from the chiral level

Even though the contribution from the chiral level is, at least schematically, covered by the reasoning above, it serves a purpose to spell it out explicitly. Initially, this reads

$$\begin{aligned}\mathrm{Im}\big[\chi^0_{xx}(\omega)\big] = -\frac{e^2v_F^2}{8\pi l_B^2}\int dk_z\Bigg(&\{\theta[\mu-E_0(k_z)]-\theta[\mu-E_{1,+}(k_z)]\}\left[1-\frac{g(k_z)}{\sqrt{g^2(k_z)+\frac{2}{l_B^2}}}\right]\delta\left\{\hbar\omega-\hbar v_F\left[g(k_z)-\sqrt{g^2(k_z)+\frac{2}{l_B^2}}\right]\right\}\\
&+\{\theta[\mu-E_0(k_z)]-\theta[\mu-E_{1,-}(k_z)]\}\left[1+\frac{g(k_z)}{\sqrt{g^2(k_z)+\frac{2}{l_B^2}}}\right]\delta\left\{\hbar\omega-\hbar v_F\left[g(k_z)+\sqrt{g^2(k_z)+\frac{2}{l_B^2}}\right]\right\}\\
&+\{\theta[\mu-E_{1,+}(k_z)]-\theta[\mu-E_0(k_z)]\}\left[1-\frac{g(k_z)}{\sqrt{g^2(k_z)+\frac{2}{l_B^2}}}\right]\delta\left\{\hbar\omega-\hbar v_F\left[\sqrt{g^2(k_z)+\frac{2}{l_B^2}}-g(k_z)\right]\right\}\\
&+\{\theta[\mu-E_{1,-}(k_z)]-\theta[\mu-E_0(k_z)]\}\left[1+\frac{g(k_z)}{\sqrt{g^2(k_z)+\frac{2}{l_B^2}}}\right]\delta\left\{\hbar\omega-\hbar v_F\left[-\sqrt{g^2(k_z)+\frac{2}{l_B^2}}-g(k_z)\right]\right\}\Bigg),\end{aligned}\tag{A21}$$

$$\begin{aligned}\mathrm{Re}\big[\chi^0_{xy}(\omega)\big] = -\frac{e^2v_F^2}{8\pi l_B^2}\int dk_z\Bigg(&\{\theta[\mu-E_0(k_z)]-\theta[\mu-E_{1,+}(k_z)]\}\left[1-\frac{g(k_z)}{\sqrt{g^2(k_z)+\frac{2}{l_B^2}}}\right]\delta\left\{\hbar\omega-\hbar v_F\left[g(k_z)-\sqrt{g^2(k_z)+\frac{2}{l_B^2}}\right]\right\}\\
&+\{\theta[\mu-E_0(k_z)]-\theta[\mu-E_{1,-}(k_z)]\}\left[1+\frac{g(k_z)}{\sqrt{g^2(k_z)+\frac{2}{l_B^2}}}\right]\delta\left\{\hbar\omega-\hbar v_F\left[g(k_z)+\sqrt{g^2(k_z)+\frac{2}{l_B^2}}\right]\right\}\\
&-\{\theta[\mu-E_{1,+}(k_z)]-\theta[\mu-E_0(k_z)]\}\left[1-\frac{g(k_z)}{\sqrt{g^2(k_z)+\frac{2}{l_B^2}}}\right]\delta\left\{\hbar\omega-\hbar v_F\left[\sqrt{g^2(k_z)+\frac{2}{l_B^2}}-g(k_z)\right]\right\}\\
&-\{\theta[\mu-E_{1,-}(k_z)]-\theta[\mu-E_0(k_z)]\}\left[1+\frac{g(k_z)}{\sqrt{g^2(k_z)+\frac{2}{l_B^2}}}\right]\delta\left\{\hbar\omega-\hbar v_F\left[-\sqrt{g^2(k_z)+\frac{2}{l_B^2}}-g(k_z)\right]\right\}\Bigg).\end{aligned}\tag{A22}$$

The integrals are again carried out by solving the expressions inside the Dirac δ distributions, which yields

$$\hbar\omega-\hbar v_F\left[g(k_z)-\sqrt{g^2(k_z)+\frac{2}{l_B^2}}\right]=0\Rightarrow g(k_z)=\frac{\omega^2l_B^2-2v_F^2}{2l_B^2v_F\omega}\theta(-\omega),\tag{A23}$$

$$\hbar\omega-\hbar v_F\left[g(k_z)+\sqrt{g^2(k_z)+\frac{2}{l_B^2}}\right]=0\Rightarrow g(k_z)=\frac{\omega^2l_B^2-2v_F^2}{2l_B^2v_F\omega}\theta(\omega),\tag{A24}$$

$$\hbar\omega-\hbar v_F\left[\sqrt{g^2(k_z)+\frac{2}{l_B^2}}-g(k_z)\right]=0\Rightarrow g(k_z)=\frac{2v_F^2-\omega^2l_B^2}{2l_B^2v_F\omega}\theta(\omega),\tag{A25}$$

$$\hbar\omega-\hbar v_F\left[-\sqrt{g^2(k_z)+\frac{2}{l_B^2}}-g(k_z)\right]=0\Rightarrow g(k_z)=\frac{2v_F^2-\omega^2l_B^2}{2l_B^2v_F\omega}\theta(-\omega).\tag{A26}$$

Plugging these solutions back into the expression for the chiral contribution, we arrive at

$$\begin{aligned}\mathrm{Im}\big[\chi^0_{xx}(\omega)\big] = -\frac{e^2v_F^2}{8\pi l_B^2}\sum_{i=1}^{m}\Bigg(&\big\{\theta\big[\mu-E_0\big(k_1^i\big)\big]-\theta\big[\mu-E_{1,+}\big(k_1^i\big)\big]\big\}\frac{\theta(-\omega)}{\hbar v_F\big|g'\big(k_1^i\big)\big|}+\big\{\theta\big[\mu-E_0\big(k_1^i\big)\big]-\theta\big[\mu-E_{1,-}(k_1^i)\big]\big\}\frac{\theta(\omega)}{\hbar v_F\big|g'\big(k_1^i\big)\big|}\\
&+\big\{\theta\big[\mu-E_{1,+}\big(k_2^i\big)\big]-\theta\big[\mu-E_0\big(k_2^i\big)\big]\big\}\frac{\theta(\omega)}{\hbar v_F\big|g'\big(k_2^i\big)\big|}+\big\{\theta\big[\mu-E_{1,-}\big(k_2^i\big)\big]-\theta\big[\mu-E_0\big(k_2^i\big)\big]\big\}\frac{\theta(-\omega)}{\hbar v_F|g'(k_2^i)|}\Bigg),\end{aligned}\tag{A27}$$

$$\mathrm{Re}\left[\chi^0_{xy}(\omega)\right] = -\frac{e^2 v_F^2}{8\pi l_B^2}\sum_{i=1}^{m}\left(\left\{\theta\left[\mu - E_0\left(k_1^i\right)\right] - \theta\left[\mu - E_{1,+}\left(k_1^i\right)\right]\right\}\frac{1}{\hbar v_F\left|g'\left(k_1^i\right)\right|} + \left\{\theta\left[\mu - E_0\left(k_1^i\right)\right] - \theta\left[\mu - E_{1,-}\left(k_1^i\right)\right]\right\}\frac{1}{\hbar v_F\left|g'\left(k_1^i\right)\right|}\right.$$
$$\left. + \left\{\theta\left[\mu - E_{1,+}\left(k_2^i\right)\right] - \theta\left[\mu - E_0\left(k_2^i\right)\right]\right\}\frac{1}{\hbar v_F\left|g'\left(k_2^i\right)\right|} + \left\{\theta\left[\mu - E_{1,-}\left(k_2^i\right)\right] - \theta\left[\mu - E_0\left(k_2^i\right)\right]\right\}\frac{1}{\hbar v_F\left|g'\left(k_2^i\right)\right|}\right), \tag{A28}$$

where $k^i_{1,2}$ denotes the solutions obtained when solving Eqs. (A23)–(A26) for k_z.

[1] K. von Klitzing, G. Dorda, M. Pepper, Phys. Rev. Lett. **45**, 494 (1980).
[2] A. Altland and M. R. Zirnbauer, Phys. Rev. B **55**, 1142 (1997).
[3] M. Z. Hasan and C. L. Kane, Rev. Mod. Phys. **82**, 3045 (2010).
[4] X.-L. Qi and S.-C. Zhang, Rev. Mod. Phys. **83**, 1057 (2011).
[5] M. O. Goerbig, Rev. Mod. Phys. **83**, 1193 (2011).
[6] N. P. Armitage, E. J. Mele, and A. Vishwanath, Rev. Mod. Phys. **90**, 015001 (2018).
[7] S.-Y. Xu, I. Belopolski, N. Alidoust, M. Neupane, G. Bian, C. Zhang, R. Sankar, G. Chang, Z. Yuan, C.-C. Lee, S.-M. Huang, H. Zheng, J. Ma, D. S. Sanchez, B. Wang, A. Bansil, F. Chou, P. P. Shibayev, H. Lin, S. Jia *et al.*, Science **349**, 613 (2015).
[8] B. Q. Lv, H. M. Weng, B. B. Fu, X. P. Wang, H. Miao, J. Ma, P. Richard, X. C. Huang, L. X. Zhao, G. F. Chen, Z. Fang, X. Dai, T. Qian, and H. Ding, Phys. Rev. X **5**, 031013 (2015).
[9] L. Lu, Z. Wang, D. Ye, L. Ran, L. Fu, J. D. Joannopoulos, and M. Soljačić, Science **349**, 622 (2015).
[10] H. Weyl, Z. Phys. **56**, 330 (1929).
[11] X. Huang, L. Zhao, Y. Long, P. Wang, D. Chen, Z. Yang, H. Liang, M. Xue, H. Weng, Z. Fang, X. Dai, and G. Chen, Phys. Rev. X **5**, 031023 (2015).
[12] X. Wan, A. M. Turner, A. Vishwanath, and S. Y. Savrasov, Phys. Rev. B **83**, 205101 (2011).
[13] P. Hosur and X. Qi, C. R. Phys. **14**, 857 (2013).
[14] A. A. Soluyanov, D. Gresch, Z. Wang, Q. S. Wu, M. Troyer, X. Dai, and B. A. Bernevig, Nature (London) **527**, 495 (2015).
[15] E. J. Bergholtz, Z. Liu, M. Trescher, R. Moessner, and M. Udagawa, Phys. Rev. Lett. **114**, 016806 (2015).
[16] M. N. Ali, J. Xiong, S. Flynn, J. Tao, Q. D. Gibson, L. M. Schoop, T. Liang, N. Haldolaarachchige, M. Hirschenberger, N. P. Ong, and R. J. Cava, Nature (London) **514**, 205 (2014).
[17] N. Kumar, Y. Sun, N. Xu, K. Manna, M. Yao, V. Süss, I. Leermakers, O. Young, T. Förster, M. Schmidt, H. Borrmann, B. Yan, U. Zeitler, M. Shi, C. Felser, and C. Shekhar, Nat. Commun. **8**, 1642 (2017).
[18] L.-K. Zeng, R. Lou, D.-S. Wu, Q. N. Xu, P.-J. Guo, L.-Y. Kong, Y.-G. Zhong, J.-Z. Ma, B.-B. Fu, P. Richard, P. Wang, G. T. Liu, L. Lu, Y.-B. Huang, C. Fang, S.-S. Sun, Q. Wang, L. Wang, Y.-G. Shi, H. M. Weng *et al.*, Phys. Rev. Lett. **117**, 127204 (2016).
[19] C.-L. Zhang, S.-Y. Xu, I. Belopolski, Z. Yuan, Z. Lin, B. Tong, G. Bian, N. Alidoust, C.-C. Lee, S.-M. Huang, T.-R. Chang, G. Chang, C.-H. Hsu, H.-R. Jeng, M. Neupance, D. S. Sanchez, H. Zheng, J. Wang, H. Lin, C. Zhang *et al.*, Nat. Commun. **7**, 10735 (2016).
[20] H. B. Nielsen, and M. Ninomiya, Phys. Lett. B **130**, 389 (1983).
[21] C.-X. Liu, P. Ye, and X.-L. Qi, Phys. Rev. B **92**, 119904(E) (2015).
[22] D. T. Son and N. Yamamoto, Phys. Rev. Lett. **109**, 181602 (2012).
[23] A. G. Grushin, Phys. Rev. D **86**, 045001 (2012).
[24] A. A. Zyuzin and A. A. Burkov, Phys. Rev. B **86**, 115133 (2012).
[25] P. Goswami and S. Tewari, Phys. Rev. B **88**, 245107 (2013).
[26] S. A. Parameswaran, T. Grover, D. A. Abanin, D. A. Pesin, and A. Vishwanath, Phys. Rev. X **4**, 031035 (2014).
[27] J. Klier, I. V. Gornyi, and A. D. Mirlin, Phys. Rev. B **92**, 205113 (2015).
[28] J. Klier, I. V. Gornyi, and A. D. Mirlin, Phys. Rev. B **96**, 214209 (2017).
[29] J. Behrends, F. K. Kunst, and B. Sbierski, Phys. Rev. B **97**, 064203 (2018).
[30] P. E. C. Ashby and J. P. Carbotte, Phys. Rev. B **87**, 245131 (2013).
[31] S. Tchoumakov, M. Civelli, and M. O. Goerbig, Phys. Rev. Lett. **117**, 086402 (2016).
[32] M. Stålhammar, J. Larana-Aragon, J. Knolle, and E. J. Bergholtz, Phys. Rev. B **102**, 235134 (2020).
[33] S. Yadav, S. Sekh, and I. Mandal, Phys. B: Condens. Matter **656**, 414765 (2023).
[34] X. Yuan, Z. Yan, C. Song, M. Zhang, Z. Li, C. Zhang, Y. Liu, W. Wang, M. Zhao, Z. Lin, T. Xie, J. Ludwig, Y. Jiang, X. Zhang, C. Shang, Z. Ye, J. Wang, F. Chen, Z. Xia, D. Smirnov *et al.*, Nat. Commun. **9**, 1854 (2018).
[35] A. V. Pronin and M. Dressel, Physica Status Solidi B **258**, 2000027 (2021).
[36] S. Polatkan, M. O. Goerbig, J. Wyzula, R. Kemmler, L. Z. Maulana, B. A. Piot, I. Crassee, A. Akrap, C. Shekhar, C. Felser, M. Dressel, A. V. Pronin, and M. Orlita, Phys. Rev. Lett. **124**, 176402 (2020).
[37] M. Udagawa and E. J. Bergholtz, Phys. Rev. Lett. **117**, 086401 (2016).
[38] Z.-M. Yu, Y. Yao, and S. A. Yang, Phys. Rev. Lett. **117**, 077202 (2016).
[39] M. Trescher, E. J. Bergholtz, M. Udagawa, and J. Knolle, Phys. Rev. B **96**, 201101(R) (2017).
[40] M. Trescher, E. J. Bergholtz, and J. Knolle, Phys. Rev. B **98**, 125304 (2018).

[41] F. Xiong, C. Honerkamp, D. M. Kennes, and T. Nag, Phys. Rev. B **106**, 045424 (2022).
[42] M. Chang, R. Ma, and L. Sheng, Phys. Rev. B **108**, 165416 (2023).
[43] H.-Z. Lu, S.-B. Zhang, and S.-Q. Shen, Phys. Rev. B **92**, 045203 (2015).
[44] X. Li, B. Roy, and S. Das Sarma, Phys. Rev. B **94**, 195144 (2016).
[45] C. M. Wang, H.-P. Sun, H.-Z. Lu, and X. C. Xie, Phys. Rev. Lett. **119**, 136806 (2017).
[46] H. Li, H. Liu, H. Jiang, and X. C. Xie, Phys. Rev. Lett. **125**, 036602 (2020).